2011

Numerical Investigation of Gas-Particle Supersonic Flow

Mihir A. Samel
University of Massachusetts Amherst

NUMERICAL INVESTIGATION OF GAS-PARTICLE SUPERSONIC FLOW

A Thesis Presented

by

MIHIR A. SAMEL

Submitted to the Graduate School of the
University of Massachusetts Amherst in partial fulfillment
of the requirements for the degree of

MASTER OF SCIENCE IN MECHANICAL ENGINEERING

September 2011

Mechanical and Industrial Engineering

NUMERICAL INVESTIGATION OF GAS-PARTICLE SUPERSONIC FLOW

A Thesis Presented

by

MIHIR A. SAMEL

Approved as to style and content by:

David P. Schmidt, Chair

Robert W. Hyers, Member

Jon G. McGowan, Member

Donald L. Fisher, Department Head
Mechanical and Industrial Engineering

To my parents, Geeta and Anil Samel.

ACKNOWLEDGMENTS

I'd like to thank Professor Schmidt for all the support and guidance provided to me during this research. I am deeply grateful to the trust and patience he has had with me, without which I probably would not have acheived this. I would like to thank my committee members, Prof Robert Hyers and Prof Jon McGowan for their valuable suggestions and insight. Let me also thank Prof Thomas Blake to grant me the opportunity to conduct this research. I would like to acknowledge all my lab mates, viz. Dnyanesh, Kshitij, Kyle, Michael Martel , Michael Colarossi, Raghu, Sandeep, Shiva, Tom and Tim and many others for their support and for the fun I had during my stay at Umass. Thanks to all the friends I made during my stay at Amherst. And above all, my greatest regards to my parents, Geeta and Anil Samel to whom I owe everything I have in life.

ABSTRACT

NUMERICAL INVESTIGATION OF GAS-PARTICLE SUPERSONIC FLOW

SEPTEMBER 2011

MIHIR A. SAMEL

B.E., UNIVERSITY OF MUMBAI

M.S.M.E., UNIVERSITY OF MASSACHUSETTS AMHERST

Directed by: Professor David P. Schmidt

Particles lying in the sub-micron range have widespread applications in the pharmaceutical, ceramic and other related industries. Separation and classification of these particles is a very important step involved in the manufacturing of these products. Inertial separation, which involves forcing a rapid change in direction of flow of a particle laden gas flow, such that the solid particles separate from the gas streamlines due to their inertia, is the most commonly applied separation technique used for industrial applications. This rapid change in direction of the fluid can be forced by rapidly accelerating the mixture to high velocity and low pressure using a sonic nozzle, causing disequilibrium between the phases. This separation property of supersonic jets, called 'aerodynamic separation', has been widely used in molecular beam formation and mass spectrometry, techniques for analyzing properties of a substance. These processes isolate a narrow beam of molecules, ions, and heavy isotopes along the centerline axis, so that the beam can be introduced in a testing chamber for their analysis.

Using Computational Fluid Dynamics (CFD), I have demonstrated how supersonic free jets can be applied for the large scale isolation and separation of sub-micron solid particles. Optimum separation for particles of a particular diameter can be obtained, in the form of a very narrow distribution along the centerline axis. This separation regime is represented by the optimum value of the dimensionless parameter called as the Stokes number (S_t), which predicts the probability of particles to separate from the gas phase after encountering an obstacle in the flow. Straight nozzles or capillaries which provide maximum acceleration at its inlet have been found to be best suited for such applications. The acceleration experienced by the gas-particle mixture due to the sudden change in area of the nozzle, is the primary factor responsible for the separation of the path of both phases.

TABLE OF CONTENTS

LIST OF TABLES

Table **Page**

LIST OF FIGURES

Figure **Page**

CHAPTER 1

INTRODUCTION

1.1 Background and motivation

Particles lying in the sub-micron range have widespread applications in the pharmaceutical, ceramic and other related industries. They also have increasing application in processes such as 'Gas dynamic cold spray process' [13,35], for the production of thin metallic films. Inertial separation is used to separate solid particles or droplets from a gas stream by enforcing a change in the velocity and direction of the gas. The particles, due to their inertia, find themselves unable to follow this change in direction and hence separate out of the gas flow. Cyclone separators have been one of the most popular categories of inertial separators on account of their simplicity in design and construction and high collection efficiency. In a typical cyclone separator the gas-solid flow in injected into a cylindrical separator chamber in a direction tangential to its circumference. This results in a vortex flow about the axis. The particles, on account of their inertia, are hurled onto the walls of the chamber. On losing their momentum because of the impact with the walls, the particles fall to the bottom of the chamber where they are collected. In spite of the wide application of cyclone separation in dust removal processes, it is difficult to obtain satisfactory collection efficiency for sub-micron particles.

Impact separators force the change in direction of the fluid by imposing an obstacle in its path. Common obstacles can come in many shapes. This obstacle causes causes a disequilibrium between the two phases, causing the particles to diverge from the gas after impacting the surface. Frain (2000) [17] designed a conical array of concentrically

arranged circular rings which obtained collection efficiency in the range of 80-85% for a particle size of 10 μm.

The separation of a particle is defined by the non-dimensional parameter called the Stokes number (S_t), which is the ratio of two time scales, τ_p and τ. The τ_p, or the particle dynamics time scale is the time required by the particle suspended in a gas, to respond to the change in velocity of the gas, after experiencing an acceleration due to the obstacle. The τ, or the gas dynamics time scale is the time taken by the gas to travel around the obstacle. Micron and sub-micron sized particles have low inertia, and hence a smaller value of τ_p and S_t. This severely affects their seperation at normal operating conditions. A review of particle dynamics in Chapter 3 shows that the value of τ_p and S_t can be increased by reducing the drag forces acting on the particles. This reduction can be achieved by operating the device at sub-atmospheric pressures. Witman (2005) [49] demonstrated this principle for particle sizes of $1 - 10\mu m$ at sub-atmospheric pressures, using a louver separator with rectangular cross-section for the blades. A collection efficiency of 85% was obtained for $1\mu m$ particles at a pressure of 0.76 torr (101 Pa.), demonstrating its potential for its application in industry.

The particle laden flow maintained at reservoir pressure conditions is introduced into the low pressure chamber through a nozzle. As the flow exits the nozzle it experiences a strong pressure gradient. Such conditions result in the formation of an under-expanded supersonic free jet. This jet is characterized by a rapid expansion of the air to operating pressure, followed by formation of shocks, such as a Barrel shock and a Mach disc. Witman's experiments were focused on the fluid and particle dynamics occuring downstream around the louver blades. However, the under-expanded jet has the potential of separating particles as they exit the nozzle, according to their diameter size.

The application of under-expanded jets is prevelant in particle analyzer systems. Both system use the properties of the jet to isolate and focus aerosol particles,

molecules or heavy isotopes along the centerline of the nozzle. In these processes, the lighter specie or the carrier gas expands as it exits the nozzle. The heavier species, representing the particles to be analyzed, however due to their relatively higher value of τ_p, continue to travel in a straight trajectory. The nozzle geometry is known to have influence on the degree of concentration of the heavy molecules around the centerline.

The size of the molecules and the ions separated in the particle analyser systems is extremely small compared to the molecules. Here, the significance of the Stokes number (S_t) is important. The value of the S_t defines the effects of fluid dynamics and the geometry of the devices on the separation of the particle and gas phases. Therefore, an optimum value of S_t shall be used to match separation performace in different conditions.

CHAPTER 2

LITERATURE REVIEW

2.1 Inertial impact particle separation

One of the earliest studies on a louver-array based inertial impact separator was conducted by Poulton and Cole (1981) [38]. The designers based the mechanism of the separation on the inertia of the solid particles suspended in the gas flow. The blade array was designed in a way that 90% of the incoming air was diverted through the blade spacing as 'clean air', while the remaining 10% with the particles continues in the original direction. The experimental results were backed up by numerical simulation of the particle trajectory using the Runge-Kutta-Merson method. The drag law acting on the particles was adopted as the one suggested by Serafini (1954) [41].

Poulton and Cole measured the performance of their device in terms of 'mass efficiency' of collection, i.e. simply by the ratio of the mass of the particles separated to the total inlet mass. Further, the variation of the collection efficiency was plotted against operating parameters such as the inlet air velocity and the design parameters such as blade thickness, pitch, and array angle. Since the designers were relying on the inertia of the particles for separation, they did not focus on the influence of the particle dynamics on collection efficiency. For example, no attention was given to study the effect operating pressure can have on the particle drag and how that can affect collection. Nevertheless, this study did successfully establish the effectiveness of louver-based separation for turbine engine applications, where the presence of solid particles suspended in the gas can cause heavy damage to the turbine blade surface.

Moreover, careful consideration to design parameters can cause minimum pressure loss across the array and hence improve the power consumption.

Musgrove et al (2009) [31] performed a computational study of a louver-based separator for application in a jet engine, in order to prevent erosion of the turbine region by solid particles in the gas. Their separator used a 'collector bin' located downstream of the louver array for particle collection. The working gas was modeled as an ideal incompressible gas, with light particle loading having no effect on the gas phase. The particle drag forces were modeled by the Haider and Levenspeil (1989) [19] drag law which expressed C_d in terms of certain empirical functions. These functions are polynomials of the shape factor ϕ, which is a measure of the sphericity, with $\phi = 1$ denoting a perfect sphere. This study recorded the collection efficiency for a range of particle diameters from 1 to 50 μm. The efficiency for different particle sizes was calculated by varying the shape factor ϕ. Perfectly spherical particles having $\phi = 1$ displayed the best collection efficiency, with a decreasing trend for lower values for ϕ (Figure 2.1). However the influence of ϕ on the particle collection efficiency was much less pronounced for particle diameter larger than 10 μm. This was attributed to the fact that for larger particles, inertia dominated the drag forces.

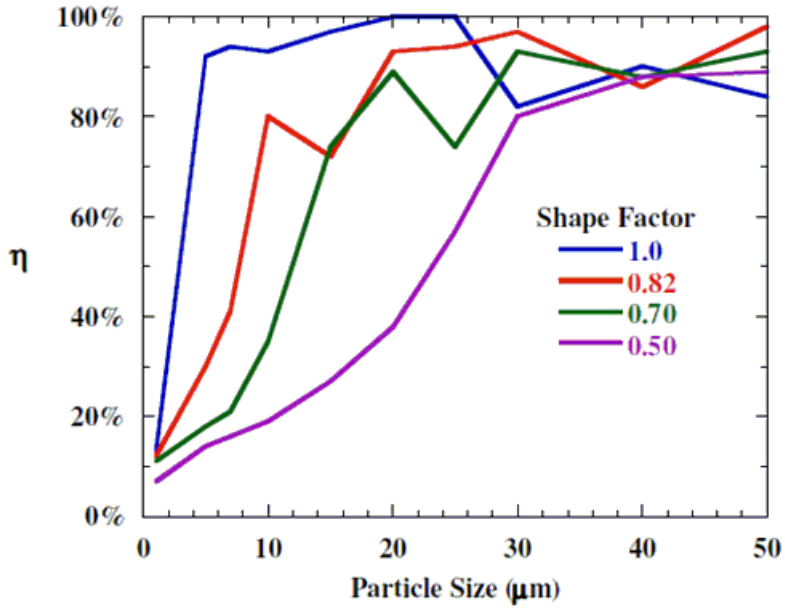

Figure 2.1. Effect of shape factor on collection efficiency, Musgrove et al [31]

Frain (2000) [17] used a conical array of concentrically arranged circular rings as the impact surface. Using the device, Frain obtained collection efficiency in the range of 80-85% for particle size of $10\mu m$. However, the efficiency dropped for particles below $10\mu m$ as these particles have a lower inertia to drag ratio due to their lower mass. Witman (2005) [49] used this mechanism for separating particles having sizes ranging from $1 - 10\mu m$ at sub-atmospheric pressures using a louver separator with rectangular configuration for the blades. A collection efficiency of 85 % was obtained for $1\mu m$ particles at a pressure of 0.76 torr $\approx$ 101 Pa demonstrating its potential for its application in industry.

In 1990, Fernandez de la Mora et al. [12], designed a hypersonic plate impactor for separation and collection of nano-sized particles. In a plate impact separator, a plate is placed close to the nozzle outlet in a direction normal to the flow. Operation of the process at normal pressures limits the value of the particle dynamics time scale(τ_p), because of the low inertia of the particles. Supersonic and hypersonic jets have regions of very low pressure which considerably reduce the drag forces on the

particles, thus producing a higher value of S_t. This enables the particles to achieve separation from the gas and collect on the plate. The nozzles used to expand the gas mixture had diameters in the range of 0.1 to 0.5 mm. The collection of the device was measured as a function of the nozzle geometry, operating conditions, and distance between the plate and the nozzle exit. The significance of these parameters was expressed through the Stokes number of the system, both in the impact region and near the nozzle exit. Successful collection efficiency was obtained for particles around 5 nm size. The collection efficiency results obtained experimentally have been used to validate the numerical solver. A detailed explanation of the validation has been offered in Chapter 5.

In (2004), Abouali and Ahmedi [1] performed computational investigation of a hypersonic 'plate impact separator' by Fernandez de la Mora et al [12]. Abouali and Ahmedi simulated the gas phase using the FLUENT compressible viscous flow solver [16]. Particle trajectories were calculated by the Stokes drag law with the Cunningham correction factor for the nano-sized particles. The mean free path (λ) of the particles was expressed in the Cunningham correction factor [11] (Equation 2.3) as a variable quantity to account for the significant variations of the values of pressure in the flow field:

$$\lambda = \frac{0.031 T^{\gamma}}{p} \tag{2.1}$$

The collection efficiency predicted by FLUENT agreed well with the experimental findings by Fernandez de la Mora et al [12], though the nozzle geometry was not included in the computational model.

The operation of particle separation methods in supersonic, rarefied conditions motivates us to take a look at how the supersonic gas flow itself can be used to separate particles based on their size. Prominent amongst these methods are molecular beam method and mass spectrometry. In these methods, molecules or heavy ions of a

given size are focused narrowly along an axis and passed into a chamber where their properties may be analyzed.

2.2 Particle focusing

The under-expanded jet is predominantly used by particle analyzer systems to separate and isolate molecules, ions of substances for analyzing their physical and chemical properties. Molecular beam method and mass spectrometry are the most prominent methods that make use of the under-expanded jet evolved due to rapid expansion of a carrier gas emerging from a sonic jet. The molecular beam method is used to isolate a stream of molecules of the carrier gas along the centerline of the nozzle, while mass spectrometry is used for the isolation of ions suspended in a lighter carrier gas. However, the principle of operation remains the same in both methods. In order to understand the application of the jet in separation of much heavier solid particles, it is necessary to conduct a brief review of both methods. Fenn [14] published an article in 2000, describing the history of the evolution of both the methods. Figure 2.2 shows the schematic representation of molecular beam methods. In the classical molecular beam method (Figure 2.2(a)), the gas effuses from source through a orifice into the collimating chamber. The beam of molecules, aligned close to the axis is generated in the collimating chamber and passed to the test chamber through a hole or a channel placed co-axially, called the 'skimmer'. However, the effusive method suffers limitations in the form of reduced beam intensity due to scattering of the molecules.

Kantrowitz and Grey [23], demonstrated that the under-expanded free jet, resulted by the expansion of a gas stored at a higher pressure reservior to an extremely low pressure region through a converging-diverging nozzle, can be used for generating molecular beams. The molecules in the beams have a very narrow velocity distribution. The pressure maintained in the low pressure expansion chamber is generally on

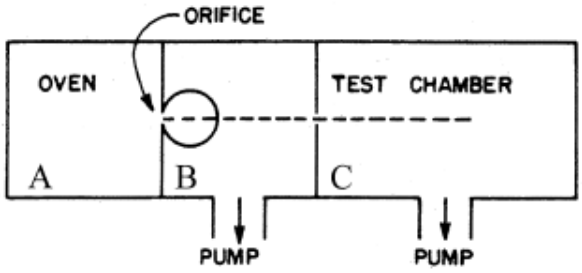

(a)

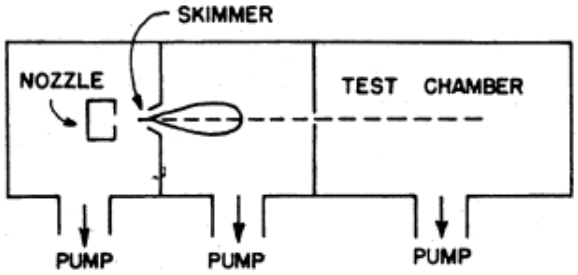

(b)

Figure 2.2. Molecular beam apparatus using (a) effusive source and (b)supersonic nozzle, Fenn [14]

the order of $100 - 400Pa$. The authors used a converging-diverging nozzle in order to obtain gas streamlines parallel to the centerline, thereby increasing the intensity of the beams. However, boundary layer effects, due to viscous flow interaction with the nozzle walls in the diverging section were observed to have a negative impact on the beam intensity. The influence of this effect was considered in the design of the nozzle geometry. Figure 2.2(b) shows a typical molecular beam apparatus using the under-expanded jet.

Becker and Bier [6] also observed the negative influence of the boundary layer effects in the diverging section of the nozzle. Moreover, they proved that removing the diverging section completely eliminated these effects and produced beam intensities much higher than the ones obtained with the diverging section. Later, Ashkenas and Sherman (1965) [4], observed that for short nozzles, without a diverging section, the viscous effects do not affect the core of the nozzle flow. They remain concentrated

in a thin boundary layer near the nozzle walls. Therefore, nozzles without diverging section (capillaries or purely converging nozzles) have been predominantly used in molecular beam formation. They are also easier to design and fabricate.

Later, Becker et al. [7] observed the property of the under-expanded jet to separate heavier species suspended in the lighter carrier gas. Becker and his team observed that when the carrier gas, contaminated with a small amount of the heavier specie, was expanded in the form of the supersonic jet, the carrier gas streamlines diverged from the centerline in a radial direction, after exiting the nozzle. However, the heavier of the species remained close to the centerline on account of their higher inertia. Hence, the specimen of the mixture, that was collected by the skimmer was enriched in the heavier of the two species. Moreover, it was observed that the skimmer, which is used to collect the separated molecular beams, enriches the beam even further, by deflecting the lighter carrier gas away. They later used this mechanism to separate heavier uranium isotopes [5]. Reis and Fenn [39] repeated such experiments to obtain hydrogen-nitrogen mixtures by using under-expanded jets as the beam sources. It was observed that the flow entering the sampling probe placed axially in the path of the jet, was enriched in the heavier species. The inertial effects at the inlet of the probe caused the species to be concentrated in the probe, while the lighter carrier medium deflected away.

The ability of a supersonic under-expanded jet to isolate heavy molecules and isotopes from a lighter carrier gas is thereby fairly known. The average size of the molecules of most elements is of an order much smaller than 1 μm, which is the desired size of this thesis. This difference in scale of the particle dimensions should be accounted for, while designing separation mechanisms for solid particles belonging to the micron range. The influence of the nozzle geometry on the flow of the gas also needs to be studied. The preceding section describes that nozzles without a diverging section to be best suited for aerodynamics separation. Hence, the attention of the

thesis will be focused on nozzle with a converging and straight section only. The above mentioned factors, viz. nozzle geometry and the operating conditions can be represented by a single dimensionless parameter called the Stokes number (S_t) which measures the probability of a particle to separate from the gas streamlines, after experience an acceleration due to an obstacle in its path. If the value of $S_t \ll 1$, the particles remain coupled to the gas streamlines after encountering the obstacle. For a value of $S_t \geq 1$, the particles separate from the gas streamlines. The S_t is given as:

$$S_t = \frac{\rho_p {d_p}^2 U}{18 \mu L} \tag{2.2}$$

where ρ_p and d_p are the particle density and diameter respectively. Here, L is the characteristic length scale in the flow, which can be represented by the nozzle diameter.

As the particles exit the nozzle into the extremely low pressure region, they experience the effects of rarefaction in form of reduction of the drag force acting on them. These effects are represented by the Cunningham correction factor (C_c), given as:

$$C_c = \left[1 + \frac{2\lambda(T,p)}{d_p}\left(1.257 + 0.4e^{-1.1\left(\frac{d_p}{2\lambda(T,p)}\right)}\right)\right] \tag{2.3}$$

where $\lambda(T,p)$ is the molecular mean free path of the particles, the distance travelled by the particle between two successive collisions. The ratio $K_n = \frac{2\lambda(T,p)}{d_p}$, called as the dimensionless parameter Knudsen number, is the ratio of the molecular mean free path to a characteristic length scale of the flow (particle diameter, d_p in this case). The magnitude of K_n signifies the regime of the flow. For sub-micron sized particles in rarefied pressure, the value of the K_n is greater than unity. This means that particles no longer move as continuum in the gas flow, but as discrete molecules amongst the gas molecules, reducing the magnitude of the drag force. The expression of the Cunningham correction factor is therefore used to obtain the computational solution of the particle trajectories.

The following sections contain a review of the characteristics of the nozzle flow, the under-expanded jet and the numerical methods to simulate the same. A brief review of inertial separation methods has been presented for the complete understanding of the principle. Further, the equations of the particle dynamics have been explained in detail in the following chapter.

2.3 Supersonic compressible flow

2.3.1 Flow in converging nozzles

The compressible flow in a converging nozzle (C-D) has been studied in detail by many authors such as Shapiro (1953) [42] and Anderson (1990) [3]. The properties of the gas across the length of the nozzle can be expressed in terms of their corresponding stagnation values and the area ratio at any point, assuming an isentropic flow. Figure 2.3 describes the isentropic flow through a C-D nozzle. The gas enters the inlet from the reservoir maintained at stagnation conditions represented by the suffix '0'. The gas reaches sonic conditions at the throat i.e. the section with minimum area. It expands isentropically to supersonic conditions in the diverging section of the nozzle. It subsequently forms an under-expanded jet as it exits the diverging section.

The Mach number of the flow can be calculated at any point across the length of the nozzle from the area of cross-section at that point and at the throat area.

$$\frac{A}{A^*} = \frac{1}{M}\left[\left(\frac{2}{\gamma+1}\right)\left(1+\frac{\gamma-1}{2}M^2\right)\right]^{\frac{\gamma+1}{2\gamma-2}} \tag{2.4}$$

The density, pressure and temperature of the gas can in turn be calculated from the local Mach number (M):

$$\frac{\rho_0}{\rho} = \left[1+\frac{\gamma-1}{2}M^2\right]^{\frac{1}{\gamma-1}} \tag{2.5}$$

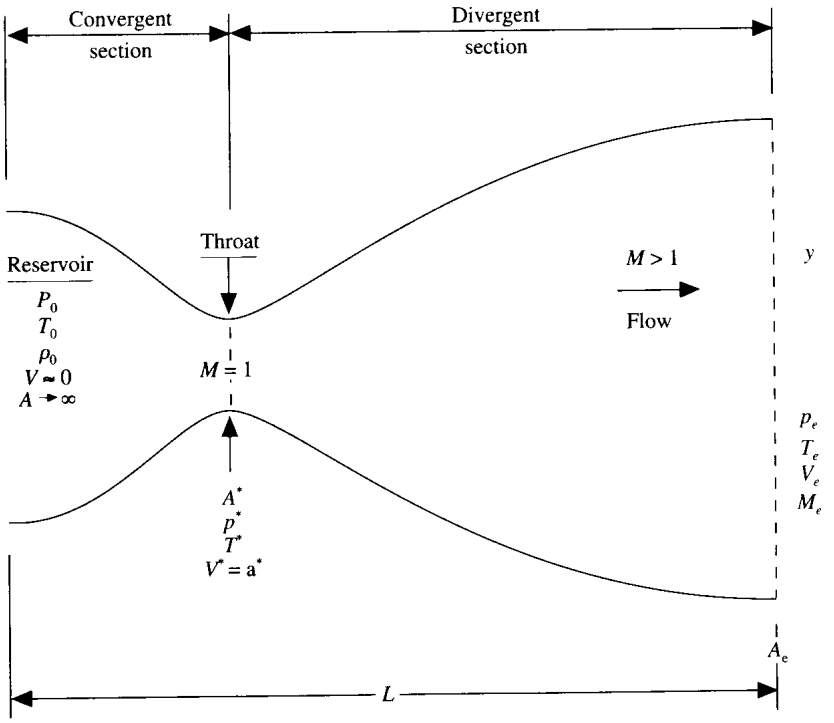

Figure 2.3. Flow in a C-D nozzle, Anderson (1990) [3]

$$\frac{P_0}{P} = \left[1 + \frac{\gamma - 1}{2} M^2\right]^{\frac{\gamma}{\gamma - 1}} \tag{2.6}$$

$$\frac{T_0}{T} = 1 + \frac{\gamma - 1}{2} M^2 \tag{2.7}$$

These equations are valid for a purely converging nozzle where sonic conditions are reached at the outlet (minimum cross-section area) of the nozzle. It must be noted however, that for sonic conditions to be reached at the outlet, the values of the outlet pressure, P_0 must be below a value represented by the "critical conditions". These conditions represented by the suffix '*' can be obtained by substituting $M = 1$ in Equations 2.5 to 2.7.

$$\frac{\rho^*}{\rho_0} = \left(\frac{2}{\gamma + 1}\right)^{\frac{1}{\gamma - 1}} = 0.6399 \tag{2.8}$$

$$\frac{P^*}{P_0} = \left(\frac{2}{\gamma+1}\right)^{\frac{\gamma}{\gamma-1}} = 0.5283 \tag{2.9}$$

$$\frac{T^*}{T_0} = \left(\frac{2}{\gamma+1}\right) = 0.8333 \tag{2.10}$$

2.3.2 Flow in constant area nozzles

Unlike converging nozzles, the compressible fluid flow through constant area nozzles cannot be governed by the change in the cross sectional area as given in Equation 2.4. The flow is driven by the pressure gradient applied across the length of the nozzle. The change in fluid properties is brought about by the friction of the gas with the nozzle walls [42]. This flow can be approximated as the "Fanno Flow". According to this approximation, if the flow at a point in the nozzle is subsonic, the effect of friction is to increase the velocity and hence decrease in pressure and density of the flow. However, if the flow is supersonic, the friction has the opposite effect on the velocity. Hence, the flow through the nozzle always tends towards $M = 1$.

2.3.3 Free under-expanded jet

The particle laden air flow is introduced into the separator chamber from a plenum chamber maintained at total pressure (P_o) through a sonic nozzle. The exit of a supersonic jet from the sonic nozzle at a pressure different from that of the external medium results in the appearance of the phenomena of Mach disc and barrel shock. When the pressure of the jet at exit (P_e) is higher than that of the ambient back pressure (P_b), the resulting jet is termed as an "under-expanded" jet. Figure 2.4 shows the structure of such a jet emerging from a converging nozzle. The flow of the gas attains $M = 1$ at the exit of the nozzle indicating choked flow. The gas at pressure P_e expands rapidly through an expansion fan, to reach P_b. As the expansion waves intercept the jet boundary, they are converted to compression waves and are deflected towards the centerline. These compression waves coalesce to form the barrel shock. Further downstream, the flow is turned parallel to the direction of the centerline through the normal shock, Mach disc. The core of the jet bounded by the barrel shock and the Mach disc is a region of very low pressure and high Mach number and is termed as the "zone of silence". This is the region from which molecular beams are extracted through the skimmer [14, 36, 40] .

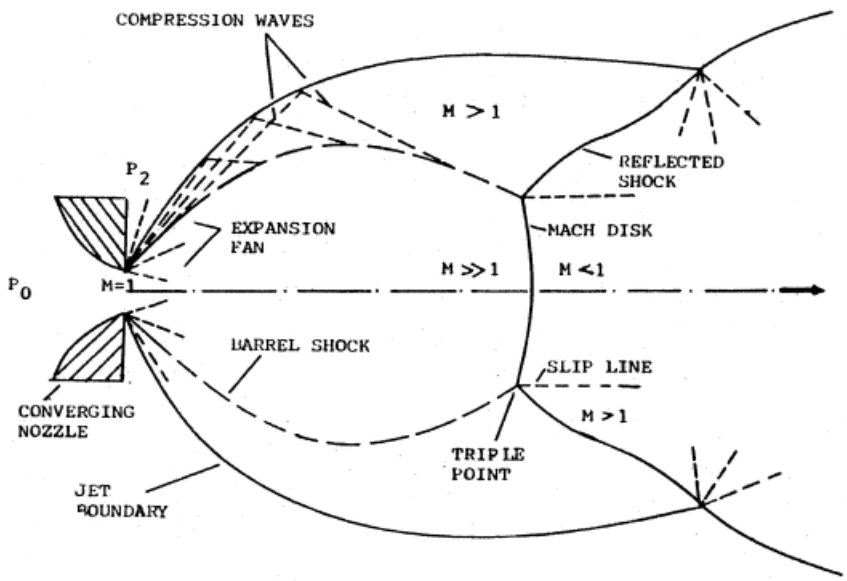

Figure 2.4. Schematic representation of the supersonic under-expanded free jet, Fenn [14]

Experimental investigation of under-expanded free jets by Crist et al (1966) [10] provided empirical expressions that expressed the Mach disc location (L_{md}) and its diameter (D_{md}), both non-dimensionalized, as a function of the stagnation pressure to ambient pressure ratio ($PR = \frac{P_o}{P_b}$) (Figure 2.5).

$$\frac{D_{md}}{D_n} = 0.36\sqrt{\left(\frac{P_o}{P_b} - 3.9\right)} \tag{2.11}$$

$$\frac{L_{md}}{D_n} = 0.65\sqrt{\left(\frac{P_o}{P_b}\right)} \tag{2.12}$$

Addy (1981) [2] performed an experimental investigation of under-expanded free-jet flows using nozzles of different geometries, with the objective of validating Crist's expressions. Experiments were conducted on one contour converging nozzle, four conically converging and a sharp-edged orifice (Figure 2.6). The diameter and location of the Mach discs were determined using 10 μs shadowgraph images. Experiments on each nozzle were conducted by varying the PR within the range of $1 \leq PR \leq 10$.

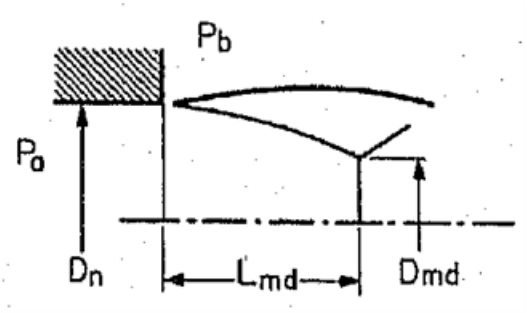

Figure 2.5. Mach Disc diameter and location for under-expanded free-jet flows Addy (1981) [2]

These experiments helped establish a plot for the onset of the Mach disc with respect to the PR for nozzles with geometries described in (Figure 2.6).

Further observations established that Crist's expressions are valid in the prediction of the location and diameter of the Mach discs for under-expanded free jet flows for all above nozzle geometries. Therefore, Addy's work has been used as a benchmark in numerous computational investigations of the same problem. Studying a free-jet computationally has been a challenge for researchers due to the series of sharp shock discontinuities present in the flow-field. Numerical schemes which are Total Variation Diminishing [20], which use a flux limiter to bound the values of the gradients around the shock to realistic values and to avoid spurious oscillations, have been most commonly used.

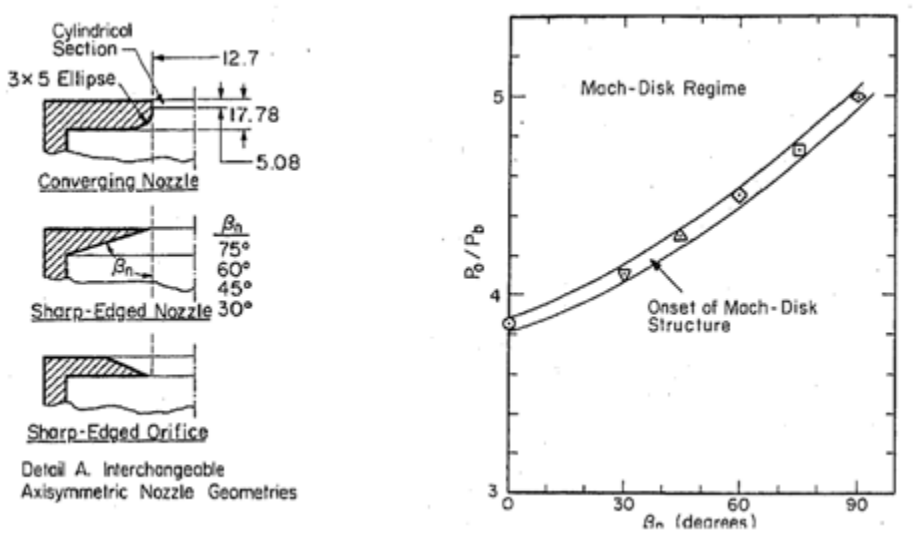

Figure 2.6. Sonic nozzle geometries and the Mach disc onset regime, Addy (1981) [2]

Murphy and Miller (1984) [30] examined the formation of under-expanded jets from converging and capillary nozzles. Pitot tube measurements at the nozzle exits revealed difference in the value of the Mach numbers obtained by both the nozzle geometries. While $M = 1$ was observed for the converging nozzle, a value of $M = 1.45$ at the exit. The properties in the downstream region were calculated using the "Method of characteristics" with the pitot tube measurements at the nozzle exit as the initial conditions. Measurements of Mach number along the centerline differed for either nozzle geometry for a distance equal to two times the nozzle diameter. However, beyond this point the profiles of the jet appeared very identical to each other.

Matsuo et al (2004) [27] studied the impact of nozzle geometry on the near field of the supersonic under-expanded jet. The free-jet characterized by the presence of a Mach disc and barrel shock were simulated by solving the Navier-Stokes [N-S] equations in axisymmetric coordinate system. A third order Total Variation Diminishing [TVD] with the MUSCL limiter [46] was implemented for the spatial derivative terms. For the discretisation of the viscous terms in the N-S equations, a second order cen-

tral differencing scheme was applied. Computational domains representing nozzle geometries used by Addy were used in order to study the influence of geometry on the appearance of the Mach disc. Each computation was performed using air as the working fluid with a value of $PR = 6.2$. The results for each nozzle case were measured in the terms of the ratios $\frac{L_{md}}{D_n}$ and $\frac{D_{md}}{D_n}$. The results successfully predicted the location and diameter of the Mach disc in the flow. However, there was no distinct presence of a barrel shock close to the exit in the case of the conically converging and the orifice nozzles. It was considered that the presence of a vena-contracta near the exit of these nozzles as a factor responsible for the distortion of the jet boundary.

Menon and Skews (2007) [28] modeled under-expanded jets using the Spallart-Allmaras turbulence model for closure of the Reynolds Averaged Navier-Stokes equations. Three different nozzle configurations were used for the computations and results were obtained for values of PR ranging from 2 to 10. The values of $\frac{D_{md}}{D_n}$ and $\frac{L_{md}}{D_n}$ were observed to be in direct variation to the value of PR, though the actual values were slightly over predicted compared to the analytical results by Addy. The authors attributed this deviation from theoretical results to the lack of account of the boundary layer formation in the nozzle geometry. They even suggested that the effects of turbulence may have a bearing on the stem heights and hence needs to be investigated. Further the Mach disc was accompanied with a slight curvature that seemed to be increasing with the PR.

Otobe et al.(2007) [34] conducted a similar study for nozzle geometries of various configurations. They chose to model their computations using the inviscid Eulerian compressible flow equations as the governing differential equations assuming that viscous effects do not have a significant influence on the flow structure. The choice of nozzle configuration was the same as used by Addy. The equations were solved using a third-order TVD finite difference scheme by Yee (1989) [50]. Grid sizes were varied to obtain grid-independent solutions. Air at atmospheric temperature and pressure was

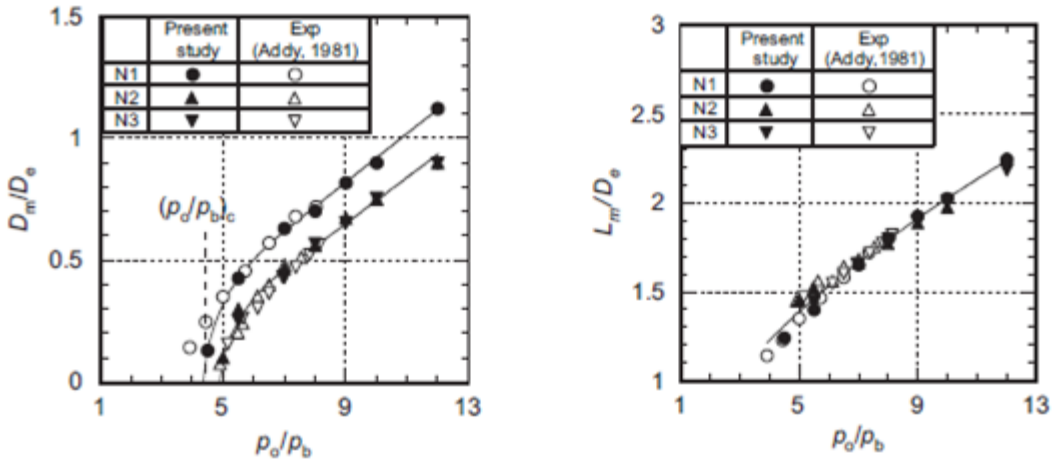

Figure 2.7. Correlation between PR and Mach disc location and stem height, Otobe [34]

assumed for inlet conditions while the back pressure was varied to study results for 4 $\leq$ PR $\leq$ 12. These results sought successful confirmation with the analytical model presented by Addy. The stem heights varied with respect to the PR. A variation for these values for the different nozzle configuration was also obtained. The location of the Mach disc was determined as a function of the PR alone and is independent of the nozzle geometry (Figure 2.7).

CHAPTER 3

PROPOSED METHODOLOGY

3.1 Eulerian phase

The simulation of the under-expanded free jet flow in the separator chamber is performed using compressible flow solver *rhoCentralFoam* [18], which is a part of OpenFOAM © [33]. High speed compressible flow is characterized by the presence of discontinuities such as shocks and contact discontinuities, the treatment of which is difficult to handle. Schemes such as the piecewise parabolic method (PPM) [9], essentially non-oscillatory (ENO) schemes [20], weighted ENO (WENO) [21] schemes have been popular in the numerical calculation of compressible flows. These schemes basically are approximate Riemann solvers that involve characteristic decomposition and Jacobian evaluation, which make them difficult to implement and are computationally expensive.

rhoCentralFoam uses an alternate Riemann-free approach that is independent of characteristic decomposition and Jacobian evaluation. This approach, named the "central scheme" described by Nessyahu and Tadmor [32], has been derived from the Lax-Friedrichs scheme. The resulting numerical method has been proved to obtain accurate and inexpensive solutions for compressible flow problems [18].

3.1.1 Governing equations

We solve the governing equations of fluid motion for the Eulerian phase. These equations are discretised and subsequently solved using the Finite-Volume method which shall be described briefly in section 3.1.2. The equations are expressed as a set

of partial differential equations (PDEs) which are derived by the application of the laws of conservation to fluid motion :

Conservation of mass (Continuity equation):

$$\frac{\partial \rho}{\partial t} + \nabla \cdot [\bar{u}\rho] = 0 \tag{3.1}$$

Conservation of momentum neglecting gravity and particle drag:

$$\frac{\partial (\rho \bar{u})}{\partial t} + \nabla \cdot [\bar{u}(\rho \bar{u})] + \nabla p + \nabla \cdot \sigma = \mathbf{0} \tag{3.2}$$

where σ is the viscous stress tensor considered positive in compression.

Conservation of energy:

$$\frac{\partial (\rho E)}{\partial t} + \nabla \cdot [\bar{u}(\rho E)] + \nabla \cdot (\bar{u}p) + \nabla \cdot (\sigma \cdot \bar{u}) = \nabla \cdot (k \nabla T) \tag{3.3}$$

where, the primary variable (ρE) is the total energy of the system, k is the conductivity and T is the temperature and $E = e + \frac{|u^2|}{2}$, where $e = c_v T = (\gamma\text{-}1)\text{RT}$ is the specific internal energy and $\gamma = \frac{Cp}{Cv}$ is the ratio of specific heats at constant pressure and constant volume.

The value of temperature is calculated as

$$T = \frac{1}{c_v} \left(\frac{\rho E}{\rho} - \frac{|u^2|}{2} \right) \tag{3.4}$$

The Equations (3.1 - 3.3) are closed by the ideal gas equation of state :

$$p = \rho R T \tag{3.5}$$

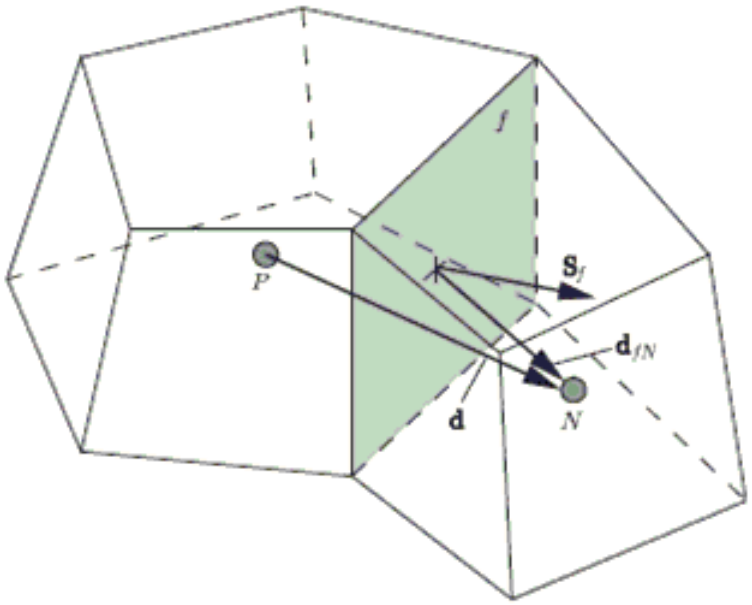

Figure 3.1. F-V control volume, Greenshields et al (2009) [18]

3.1.2 Finite volume method

In the Finite-Volume method [47] the computational domain is divided into polyhedral cells called Control Volumes (CV). Figure 3.1 shows a typical control volume. Neighboring CVs are connected to each other by a face f represented by the area vector S_f .The vector S_f points normally outwards from the cell designated as the "owner cell". The cell that shares the face f with "owner cell" is named as "neighboring cell" for the sake of convenience. The cell centers of the owner and neighboring cells (named P and N respectively) are connected by the vector $\bar{d}$. The governing PDE's are integrated over the CVs. Gauss' theorem is implemented to convert these integrals into surface integrals over the face f.

Discretisation is the next step where the surface integrals are converted into a set of simple algebraic equations involving values of the flux of the primary variables ψ_f. The values on the face of the CV are interpolated from values at centers (ψ_P and ψ_N) of the cells connected by that face. The detailed procedure of discretisation and interpolation has been explained in the following sections.

3.1.2.1 Discretisation of convective terms

The convective terms in Eqns (3.1 - 3.3) are $\nabla \cdot [(\bar{u}\rho)], \nabla \cdot [\bar{u}(\rho\bar{u})]$ and $\nabla \cdot [\bar{u}(\rho E)]$. Each term is integrated over the control volume and further linearized as follows:

$$\int_V \nabla \cdot (\bar{u}\psi) dV = \int_S dS \cdot (\bar{u}\psi) = \sum_f \phi_f \psi_f \tag{3.6}$$

where ϕ_f=S$_f$.$\bar{u}_f$ is the volume of fluid passing through the face per unit time. *rhoCentralFoam* uses a non-staggered central differencing interpolation scheme by Kurganov, Noella, Petrova [25] to obtain ψ_f by splitting the flux in two directions, namely incoming and outgoing directions. The quantities shall be represented by the suffixes, $f-$ and $f+$ respectively.

The discretisation can be represented thereby as :

$$\sum_f \phi_f \psi_f = \sum_f [\alpha \phi_{f+} \psi_{f+} + (1-\alpha)\phi_{f-}\psi_{f-}] \tag{3.7}$$

ϕ_f in either direction is calculated from the respective local speeds of propagation:

$$\phi_{f+} = |S|\, max[(\bar{u}_{f+} + c_{f+}), (\bar{u}_{f-} + c_{f-}), 0] \tag{3.8}$$

$$\phi_{f-} = |S|\, max[(\bar{u}_{f+} - c_{f+}), (\bar{u}_{f-} - c_{f-}), 0] \tag{3.9}$$

where $c_f\pm = \sqrt{\gamma RT}$ are the speeds of sound at the face for the waves in the outward and inward direction. The weighting function α is calculated as :

$$\alpha = \frac{\phi_{f+}}{\phi_{f+} + \phi_{f-}} \tag{3.10}$$

3.1.2.2 Discretisation of gradient terms

$$\int_V \bar{\nabla}\psi dV = \int_s dS\psi = \sum_f S_f\psi_f \tag{3.11}$$

After converting the volume integral into a surface integral, the discretisation is carried out as follows:

$$\sum_f S_f\psi_f = \sum_f [\alpha S_f\phi_{f+} + (1-\alpha)S_f\phi_{f-}] \tag{3.12}$$

The fluxes in the either direction are calculated in the same procedure used for the convective terms.

3.1.2.3 Discretisation of Laplacian terms

The Laplacian terms are discretised as follows:

$$\int_V \nabla\cdot(\gamma\nabla\psi)dV = \int_S dS\cdot(\gamma\nabla\psi) \approx \sum_f \gamma_f S_f\cdot(\nabla\psi)_f \tag{3.13}$$

The diffusion constant γ_f is interpolated directly from the cell centers. The evaluation of the diffusion flux $S_f.(\nabla\psi)_f$ is split into orthogonal and non-orthogonal components.

3.1.2.4 Discretisation of temporal terms

The temporal terms in the Equations $(3.1-3.3)$ are discretised using the Euler explicit scheme:

$$\int_V \frac{\partial\psi}{\partial t} = \frac{(\psi^{n+1}-\psi^n)\,dV}{\delta t} \tag{3.14}$$

where δt is the time step

3.1.3 Boundary conditions

Numerical simulations of compressible flow problems require a delicate treatment of the boundary conditions at the inlet and the outlet. As mentioned earlier the solution of high velocity compressible flow problems has a wave-like nature. Each of these waves has a local speed of propagation which can be obtained as an eigenvalue of the Jacobian matrix of the Navier-Stokes equations. Performing a characteristic analysis of the equations to yield the eigenvalues will help to understand their significance in specifying the boundary conditions. The detailed procedure for the same has been presented by Poinsot and Lele [37]. The eigenvalues for a 3-D compressible flow system obtained as a result of the procedure can be expressed as follows:

$\lambda_1 = u - a,$

$\lambda_2, \lambda_3, \lambda_3 = u$

$\lambda_3 = u + a$

where λ_1 is the eigen value obtained for the density equation. λ_2, λ_3, λ_4 are the eigenvalues corresponding to the mometum equatios. λ_5 is the eigenvalue for the energy equation. The polarity of the values of λ_i denotes the direction of flow of the corresponding waves. The local speed of sound is denoted as 'a'. If the wave enters the computational domain at a particular boundary, its "region of dependence" lies outside the domain, which means that it relies on information that is not present in the domain. Hence the values of the variable attached to that wave needs to be specified at that boundary. On the contrary, the waves that exit the computational domain have a "region of dependence" that lies entirely inside and thereby the value of the variables at the boundary must not be specified. The following boundary conditions are encountered during the simulation of an under-expanded supersonic jet:

Inlet: Supersonic conditions are present at the inlet. All the eigenvalues of the system at the inlet have values greater than 0. This means that they enter the domain.

For such a system value for every variable viz. p, T, U needs to be specified at the inlet boundary.

Outlet: Subsonic conditions are prevalent at the outlet due to which the eigenvalue, $\lambda_1 = u - a < 0$. In order to deal with this incoming wave associated with the pressure boundary condition, non-reflective boundary conditions shall be used. The values of U and T, are allowed to float.

3.2 Discrete particle phase

The fluid-particle interaction is defined in the form of adding a source added to the Navier Stokes (N-S) equations of momentum conservation.

$$\frac{\partial \rho \bar{u}}{\partial t} + \nabla \cdot [\bar{u}(\rho \bar{u})] + \nabla p + \nabla \cdot \sigma + \sum_{\mathbf{N}} \mathbf{f_P} = \mathbf{0} \tag{3.15}$$

The nature of this fluid-particle coupling can be classified in three categories based on the concentration of the particles in the gas, in terms of the volume fraction.

1-way coupling: A dilute suspension which has a volume fraction less than 10^{-6} has negligible effect on the momentum of the gas phase i.e. the gas influences the particles, but the particles have no effect on the gas. The source term in the N-S equation can thereby be neglected.

2-way coupling : a particle suspension of volume fraction in the range of 10^{-6} to 10^{-3} influences the gas phase. The source term is added in the N-S equation to account for this 2-way coupling.

4-way coupling: for higher concentration particle-to-particle interaction must also be taken into account.

A 1-way coupling between both the phases, neglecting the effect of the particle phase on the gas phase.

3.2.1 Lagrangian equations of motion

The particle motion can be described by the following differential equation in a Lagrangian frame of reference.

$$m_p \frac{dU_p}{dt} = F_d + F_g \tag{3.16}$$

Where F_g is the force of gravity acting on the particle which shall be neglected as it is extremely small compared to the drag force. The force F_d is the drag force per unit mass of the particle, which can be expressed as:

$$F_d = \frac{1}{2} C_d A \rho_g (U - U_p) \left| U - U_p \right| \tag{3.17}$$

where C_d is the coefficient of drag, A is the projected frontal area of the particle, ρ_g is the gas density, U is the velocity of the gas, U_p is the velocity of the particle and m_p is the mass of the particle.

For a spherical particle of diameter d_p,

$$A = \frac{\pi {d_p}^2}{4} \tag{3.18}$$

$$m_p = \frac{\pi \rho_p {d_p}^3}{6} \tag{3.19}$$

Hence Eq. 3.17 for a sphere reduces to:

$$\frac{dU_p}{dt} = \frac{3}{4} \frac{C_d \rho_g}{\rho_p d_p} (U - U_p) \left| U - U_p \right| \tag{3.20}$$

Stokes (1851) [44] expressed the coefficient of drag on a spherical particle submerged in a creeping flow as:

$$C_{DS} = \frac{24}{R_{ep}} = \frac{24}{\rho_p d_p \left| U - U_p \right|} \tag{3.21}$$

After substituting ρ_g from Equation 3.19 , we derive the equation of the acceleration acting on the particle as :

$$\frac{dU_p}{dt} = \frac{C_d}{C_{DS}} \frac{18\mu}{\rho_p {d_p}^2} (U - U_p) = \frac{C_d}{C_{DS}} \frac{(U - U_p)}{\frac{\rho_p {d_p}^2}{18\mu}} \tag{3.22}$$

C_d is the actual coefficient of drag acting on the particles. Necessary corrections must be applied to Equation 3.22 in order to account for the influence of factors such as particle geometry and gas properties. Some of the available drag laws have

been reviewed in the following section. This expression for drag force also yields an important parameter $\tau_p = \frac{\rho_p {d_p}^2}{18\mu}$ which is the result of the ratio of the particle inertia to the drag called as the particle dynamics time scale, τ_p . This time scale describes the aerodynamic response time of the particle in the gas flow. The other relevant parameter is the gas dynamics time scale τ that represents the time for the gas to travel a characteristic length L with velocity U.

$$\tau = \frac{L}{U} \tag{3.23}$$

The ratio of the two time scales yields the non-dimensional parameter called as the Stokes number.

$$S_t = \frac{\tau_p}{\tau} = \frac{\rho_p {d_p}^2 U}{18 L \mu} \tag{3.24}$$

For $S_t \gg 1$, the particles separate from the air flow after the impact on the louver and escape out of the chamber through the collected outlet placed above the louver. For $S_t \ll 1$ the particles follow the air streamline closely as the air flows around the blades into the classified outlet.

3.2.2 Review of drag correlation

3.2.2.1 Drag correlation for smooth spherical particles

Morsi and Alexander [29] proposed the following relation for the drag coefficient of smooth spherical particles:

$$C_d = a_1 + \frac{a_2}{R_{ed}} + \frac{a_3}{{R_{ed}}^2} \tag{3.25}$$

Where a_1, a_2, a_3 are constants specified over several discrete ranges of R_{ed}.

3.2.2.2 Drag correlation for non-spherical particles

Haider and Levenspeil [19] expressed a drag law in the following expression

$$C_d = \frac{24}{R_e}(1 + b_1 {R_e}^{b_2}) + \frac{b_3 R_e}{b_4 + R_e} \tag{3.26}$$

where $b_1 = exp(2.3288 - 6.4581\phi^2 + 2.4886\phi^3)$

$b_2 = exp(0.0964 + 0.5565\phi^2)$

$b_3 = exp(4.094 - 13.8944\phi + 18.4222\phi^2 - 10.2599\phi^3)$

$b_4 = exp(1.4681 - 12.2584\phi - 20.7322\phi^2 + 15.8855\phi^3)$

Where ϕ= shape factor, is the measure of the sphericity of the particles. A value of $\phi = 1$ represents a perfectly spherical particle. The shape factor of the particles has been observed to have an effect on the collection efficiency. Lower shape factor tends to increase the drag acting on particles. This has a negative effect on the collection efficiency. However, since inertia dominates the flow of larger particles, the effect of ϕ on the efficiency is less pronounced on larger particles.

3.2.2.3 Drag correlation for sub-micron particles

For sub-micron spherical particles the C_d is obtained by obtained by applying the Cunningham's correction factor [11] C_c, represented in Equation 2.3. The effective expression of C_d is therefore given as follows:

$$C_d = \frac{24}{R_e C_c} = \frac{24}{R_e \left[1 + \frac{2\lambda(T,p)}{d_p}\left(1.257 + 0.4e^{-1.1\left(\frac{d_p}{2\lambda(T,p)}\right)}\right)\right]} \tag{3.27}$$

3.2.2.4 Drag correlation for supersonic rarefied flow

Henderson (1976) [22] presented a set of empirical relations to model drag forces in various flow regimes, continuum, rarefied and transition. Three equations, each representing a particular range of Mach number were derived. The first expression for subsonic flow is as follows:

$$C_d = 24\left[R_e + S\left[[4.33 + 1.567\exp\left(-0.247\frac{R_e}{S}\right)\right]\right]^{-1} A + B \tag{3.28}$$

$$A = e^{\frac{0.5M}{\sqrt{R_e}}}\left[\frac{4.5 + 0.38(0.03R_e + 0.48\sqrt{R_e})}{1 + 0.03R_e + 0.48\sqrt{R_e}}\right] \tag{3.29}$$

$$B = \left[1 - e^{\left(\frac{M}{R_e}\right)}\right] 0.6S \tag{3.30}$$

For supersonic flow with Mach number exceeding 1.75 the following expression was considered valid:

$$C_d = \frac{0.9 + \frac{0.34}{M^2} + 1.86(\frac{M}{R_e})^{0.5}\left[2 + \frac{2}{S^2} + \frac{1.058}{S} - \frac{1}{S^4}\right]}{1 + 1.86(\frac{M}{R_e})^{0.5}} \tag{3.31}$$

Where, $S = M\sqrt{(\frac{\gamma}{2})}$ is the molecular speed ratio and the ratio $\frac{R_e}{S} \approx K_n$. M is the Mach number and γ is the ratio of the specific heats.

The values of M and R_e are both based on the relative velocity between particle and fluid. For Mach number between 1 and 1.75, linear interpolation is used. The author validated the values of drag coefficient calculated by the above experiments with alternate expressions and experimental data. In continuum, rarefied and transition regimes, Henderson's expressions agreed more closely with the experimental data than other expressions.

3.2.3 Selection of drag correlation

The Stokes-Cunningham drag correlation with the Cunningham correction factor C_c has been used widely used for modeling the flow of sub-micron particles which falls in the free molecular regime. Henderson's equations are more comprehensive than the Cunningham correction factor as they include compressibility due to high Mach number flow. However, for free molecular flow, rarefaction effects dominate effects due to compressibility. This was clearly observed by Tedeschi, Gouin, Elena

(1999) [45] in their investigation of particle motion in high speed flows. Experimental values of particle velocity across a shock were compared with values calculated by theoretical expressions provided by various drag laws. The predictions by Cunningham correction factor showed satisfactory confirmation with experimental data. Moreover its expression is much simpler and hence is selected for our purpose.

CHAPTER 4

IMPLEMENTATION

The computational method for the solution of high speed compressible flow problems, described in the previous chapter has been implemented in the OpenFOAM solver *rhoCentralFoam*. OpenFOAM is a collection of C++ libraries. It uses inheritance and template features of Object Oriented Programming to design the structure of the solvers in a manner that resembles that of the actual system equations and is therefore easy to interpret. For example, the solution of the continuity equation (Equation 3.1) can be represented by the following syntax:

```
solve(
  fvm::ddt(rho) + fvc::div(phi) ==0
  );
```

This operation casts the PDE into a matrix system of the form $[A][x] = [b]$, where $[A]$ is composed of the algebraic coefficients derived from the discretisation of the convective, gradient and Laplacian terms. $[x]$ is the matrix of the dependent variables and $[b]$ is the matrix resulting from the source terms.

In order to calculate the discrete phase particle trajectories, an OpenFOAM Lagrangian particle class has been coupled with *rhoCentralFoam*. A new subroutine for the calculation of the drag force on the particles by the Cunningham correction factor has been written. We thus have an integrated compressible flow-discrete phase CFD solver that has been used to perform CFD simulations of the validation cases and the final results.

4.1 Iterative algorithm for *rhoCentralFoam*

The viscous momentum and energy equations are solved using the time-splitting approach. In this approach, the inviscid equations are solved explicitly, by the 'fvc::' operator, to obtain a predicted value of the variable. Later, the diffusion terms are then introduced as implicit corrections to the original inviscid equations, represented by the 'fvm::' operator .

The solution starts with the calculation of $\rho_{f\pm}, T_{f\pm}$ and $u_{f\pm}$ at the face of the cell, split into outgoing and incoming directions. The face values are interpolated from the values at the cell centers and substituted in the calculation of the convective fluxes. This method has been described in Equations (3.7 to 3.11).

Thereafter, the continuity equation (Equation 3.1) is solved to obtain the density, ρ. The predicted value of the velocity, $(\tilde{u})$ is calculated explicitly from the inviscid momentum equation:

$$\frac{(\tilde{\rho u}) - (\rho u)^n}{\partial t} + \nabla \cdot [u(\rho \mathbf{u})] + \nabla p = 0 \tag{4.1}$$

$$\tilde{u} = \frac{(\tilde{\rho u})}{\rho} \tag{4.2}$$

The value of $\tilde{u}$ is then used to calculate the corrected value of velocity at the next time step (denoted as n+1) implictly, from the viscous momentum Equation 3.2.

$$\frac{(\rho u)^{n+1} - (\tilde{\rho u})}{\partial t} - \nabla \cdot (\mu \nabla u) = 0 \tag{4.3}$$

The energy equation is solved in the similar manner. A predictor value of the energy flux $(\tilde{\rho E})$ is first calculated from the inviscid energy equation.

$$\frac{\partial(\rho \mathbf{E})}{\partial t} + \nabla \cdot [u(\mathbf{E} + \mathbf{p})] + \nabla \cdot (\sigma \cdot \mathbf{u}) = \mathbf{0} \tag{4.4}$$

The temperature, T is obtained using Equation 3.4, which takes ρ, u and $\mathbf{E}$ as input. The estimated value of T is then used in the corrected energy equation:

$$\frac{\partial(\rho c_v T)}{\partial t} - \nabla \cdot (k \nabla T) = 0 \tag{4.5}$$

The pressure is then updated using the ideal gas equation of state (Equation 3.5).

Sutherland's law of viscosity is used to model the viscosity μ:

$$\mu = \mu_{ref} \frac{T^{1.5}}{T + T_{ref}} \tag{4.6}$$

T = 110.4 K is the reference temperature. $\mu_{ref} = 1.716 \times 10^{-5} \frac{N.s}{m^2}$ is the reference viscosity.

4.2 Lagrangian particle class

The Lagrangian particle tracking is performed using an intermediate particle class that models effects due to kinematic, thermal and reacting forces acting on a particle. Besides, it offers flexible models for drag forces, particle injection and wall interaction models.

4.2.1 Lagrangian parcels and clouds

A physical particle is represented in the computational domain as a parcel. A computational parcel represents a number of physical particles. It is assumed to have the same velocity and material properties as the physical particle.

A cloud is a collection of Lagrangian parcels. The entire mass of particles entering the computational domain is initialized as a cloud. The Lagrangian cloud named as the *kinematicCloud1* is directly coupled with the Eulerian gas phase through the momentum equation (Equation 3.15), representing the source due to particle momentum and the gravity acting on the particles:

```
solve {
   (
     fvm::ddt(rho, U) - fvc::ddt(rho,U)
   - fvm::laplacian(mu, U)
   - fvc::div(tauMC)
  == kinematicCloud1.SU1()
   + rho.dimensionedInternalField()*g
   );
     rhoU = rho*U;
      }
```

However, it must be noted that our research assumes a one way coupling between the gas and particle phase and that the effects of gravity are totally neglected. Instead

only the values of the quantities of the gas phase are used to calculate the particle trajectories.

The *kinematicCloud* is constructed with inputs such as references to gas properties and the material properties of the particles. The quantities of the gas phase are stored at the cell centres of the Finite Volume mesh. The values of the quantities at the position of the Lagrangian particle is interpolated from the nearest cell centres, using the 'vpi' interpolator function:

```
basicKinematicCloud kinematicCloud1
    (
        "kinematicCloud1",
        vpi, %
        rho, p, T, U,mu(),  % references to gas phase.
        g   % acceration due to gravity (optional)
    );
```

The motion of the particles suspended in the high speed compressible gas flow is calculated by set of Ordinary Differential Equations [ODEs]. The position of the center of a particle, x_p is calculated by the following equation:

$$\frac{dx_p}{dt} = U_p \tag{4.7}$$

where U_p is the velocity of the particles calculated by :

$$m_p \frac{dU_p}{dt} = \sum f_p \tag{4.8}$$

where m_p is the mass of the particle. Here, $\sum f_p$ is the sum of forces acting on the particle, also representing the source term in Equation 3.15. The most dominant forces acting on a particle travelling in a gas are usually the drag forces F_d, lift forces

F_l and the forces due to Brownian motion, F_b. The flow of sub-micron particles is however dominated by the drag forces. Lift forces and Brownian forces have been found to have negligible influence, and thereby are excluded from the calculations.

$$F_d = -m_p \frac{(U_p - U)}{\tau_p} \tag{4.9}$$

where $\tau_p = \frac{4}{3} \frac{\rho_p d_p}{\rho_g C_d |U - U_p|}$ is the particle relaxation time scale.

C_d is the drag coefficient modeled using the Cunningham correction factor.

4.2.2 Particle-wall Interaction

The intermediate Lagrangian class offered by OpenFOAM has the standard wall interaction model, based on the coefficients of restitution, (e_n) and (e_t) for the normal and the tangential components respectively, of the velocity of the particle impacting on a wall. The components of the velocity are updated as follows:

$$U_{n,2} = e_n U_{n,1} \tag{4.10}$$

$$U_{t,2} = e_t U_{t,1} \tag{4.11}$$

A value of 1.0 for either e_n and e_t signifies total conservation of velocity. A value of 0.0 signifies total loss of velocity after impact with the wall. Hence the particles stick to the wall. These latter conditions represent the "Trap" boundary conditions for the particle phase and shall be used in the validation test case in Chapter 5.

CHAPTER 5

VALIDATION

5.1 Compressible flow

The introduction of supersonic flow from a sonic nozzle into a quiescent medium maintained at an ambient pressure much less than the pressure at the outlet of the jet, results in the formation of a free- under-expanded jet at the outlet of the nozzle. The details of this phenomenon have been explained in Chapter 2. Numerical simulation of this phenomenon for high inlet to ambient pressure ratio (P.R.), is a challenge due to the presence of high gradients in the flow field. Hence, it is necessary to validate the ability of the compressible flow solver, to accurately predict such flows.

The experimental study on under-expanded jets by Addy [2] provides a very reliable reference for measuring CFD predictions of the same. The objectives of the validation can therefore be explained as:

1. To verify that the solver can successfully resolve shock discontinuities across the flow field.

2. To verify the accuracy of the solution by measuring placement and dimensions of the Mach disc against analytical Eqs. (2.11) and (2.12).

5.1.1 Validation case

The validation has been performed using a rectangular mesh representing the expansion chamber outside the nozzle exit. The geometry is 50 mm long and 15 mm wide with a nozzle outlet radius 2.5 mm. The model has been meshed using 3000 cells as shown in Fig 5.1.

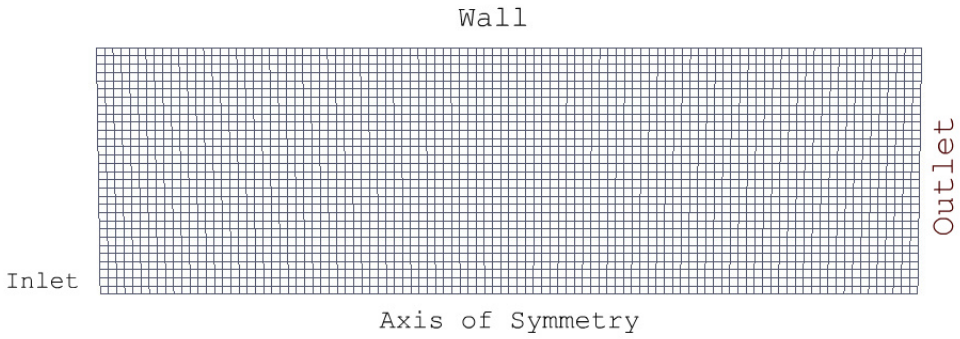

Figure 5.1. 2-D axisymmetric mesh of expansion chamber used in the validation case

Inlet boundary conditions represent sonic conditions at the nozzle exit having a total pressure of 101325 Pa, total temperature of 298 K and velocity equivalent to Mach number 1. Non-reflective outlet boundary conditions are used at the outlet, with values varied for every case (Table 5.1.1), in order to check the results for a range of pressure ratios.

5.1.2 Results

Steady state solution for the case number 3 has been plotted in 5.2(b). Fig 5.2(a) represents results for identical operating conditions obtained by Sommerfeld [43] using shadowgraph technique. The numerical results show very good agreement with

Table 5.1. Boundary conditions for validation cases

Case	p_{outlet}	Pressure ratio
1	12666	8
2	6755	15
3	3753	27
4	2533	40

the experimental results. The location and width of the Mach disc, both non-dimensionalized with respect to d_n, has been recorded for all cases and compared with Addy's empirical equation. Satisfactory agreement can again be observed between either results can be observed in Figures 5.3 and 5.4.

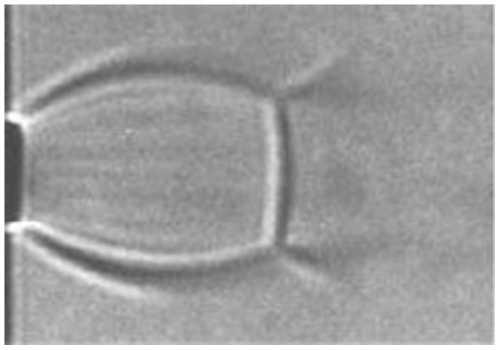

(a)

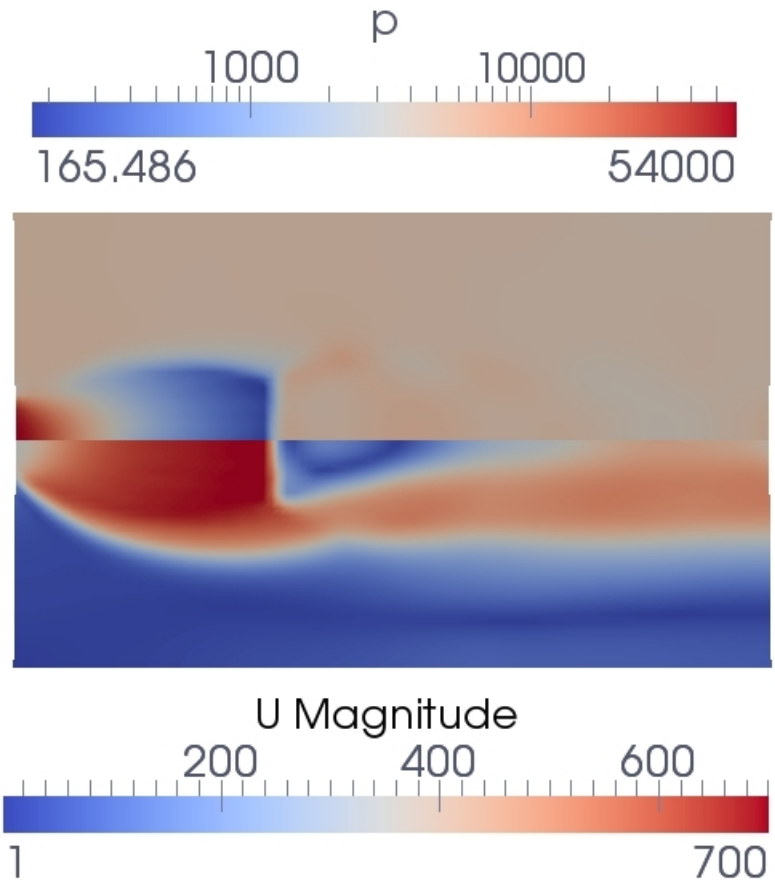

(b)

Figure 5.2. (a) Shadowgraph image [43] and (b) Steady state numerical results of under-expanded jet for $\frac{P_o}{P_b}$=27. Top half represents pressure in Pa (top scale), bottom half represents velocity in m/s (bottom scale).

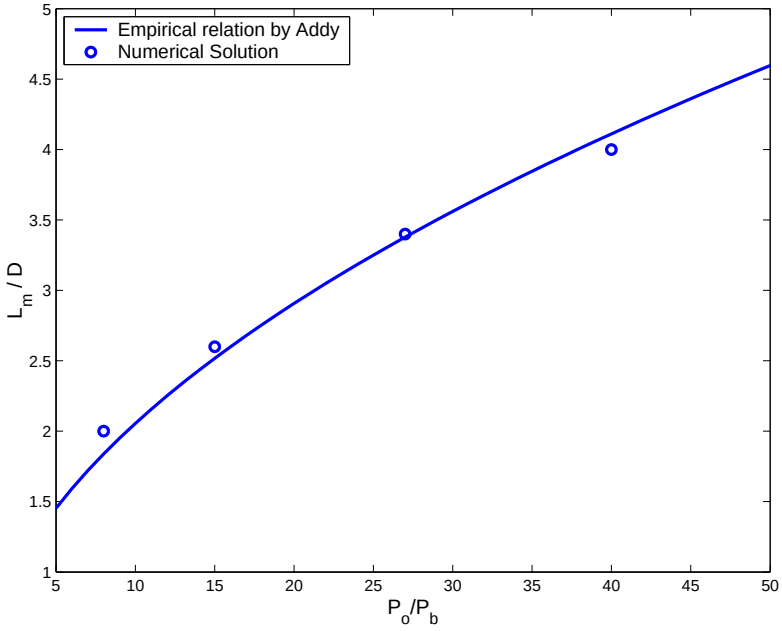

Figure 5.3. Mach disc location

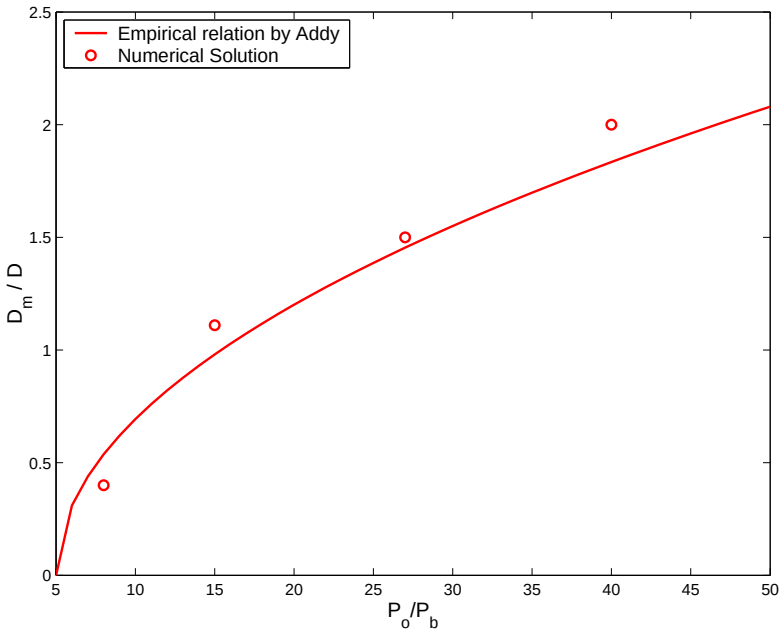

Figure 5.4. Mach disc diameter

5.2 Validation of the Cunningham correction factor (C_c)

5.2.1 Introduction

Fernandez de la Mora (1990) [12] designed a hypersonic impact separator for nano sized aerosol particles using a flat plate for the collection of the particles. The impactor plate was placed normal to the flow exiting a purely converging nozzle. In the original experiment, the distance of the plate from the nozzle exit (L_p) was varied with respect to the nozzle exit diameter (d_n) in order to check the influence of the ratio, $\frac{L_p}{d_n}$ on the collection efficiency. The results obtained for $\frac{L_p}{d_n} = 3$ are used for the validation of the OpenFOAM Lagrangian class implementing the C_c for sub-micron sized particles in rarefied flow. The original article makes no mention of the geometry of the nozzle. The nozzle used for the simulations in this case has a purely converging section with an angle of 45°. It has an outlet radius of 0.135 mm. The 2-D axisymmetrical computational mesh for the impactor is given in Figure 5.5.

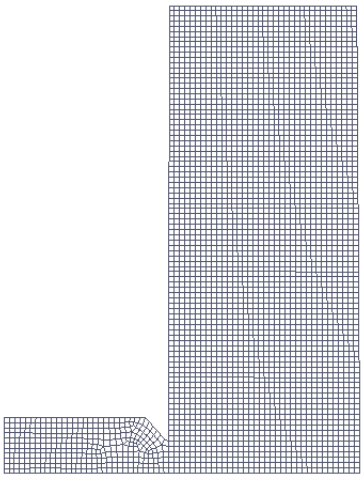

Figure 5.5. Mesh used for validation case for the Cunningham correction factor

5.2.2 Numerical results

The inlet pressure was fixed at 1 atm, with a temperature of 298 K throughout the domain. The outlet pressure was fixed at 253 Pa, consistent with experimental conditions. The single phase gas flow was calculated using the solver *rhoCentralFoam*.

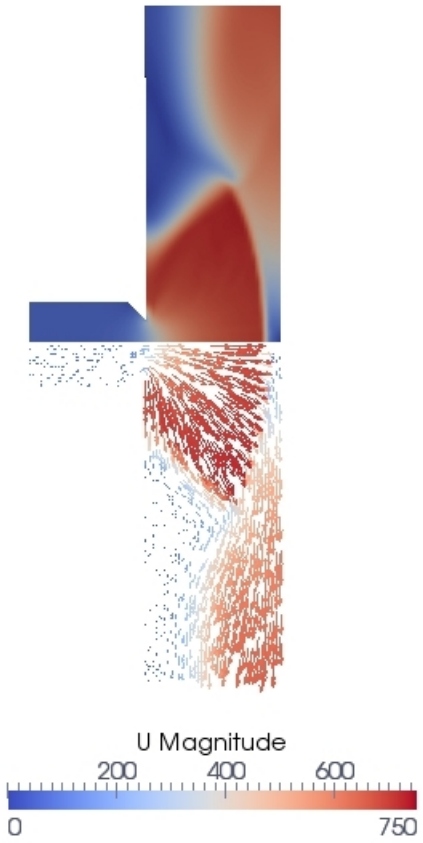

Figure 5.6. Velocity contours and vectors of the hypersonic impact separator

The velocity contours and vectors of the steady state numerical solution are plotted in Figure 5.6. The flow expands rapidly as soon as it exits the nozzle. The core of the expanded jet has very high velocity. As the jet impacts the plate, a strong shock develops in front of it. This is the bow shock, which is a form of the Mach Disc, the normal shock that accompanies an under-expanded jet facing no obstacle in its path. The impactor plate deflects the jet outwards in a radial direction. The velocity decreases rapidly across the bow shock. Variations of the Mach number of the flow

field across the centerline are plotted in Figure 5.7. The jet achieves a highest Mach number above 4. As it crosses the bow shock, the value of M_a falls rapidly.

If the distance between the plate and the nozzle exit (L_p) is infinite compared to the nozzle diameter d_n, the expansion of the air from the nozzle would take the form of the typical underexpanded jet discussed in previous sections. The location of the bow shock with respect to the nozzle exit diameter, L_{md} would be determined by Addy's expressions (Equations 2.11 and 2.12). In this case however, the location of the bow shock is the function of the nozzle geometry and the value of the ratio $\frac{L_p}{d_n}$. Fernandez de la Mora established the location of the bow shock as a function of the variable η given as :

$$\eta = \left(\frac{L_p}{d_n}\right) / \sqrt{PR} \tag{5.1}$$

The distance between the bow shock and the plate surface, at a point of the centerline axis is given as :

$$\frac{\delta}{L_p} = 1 - \frac{0.67}{\eta} \tag{5.2}$$

However, this equation only holds true for values of $\frac{L_p}{d_n} \geq 14$, as for lower values δ has a negative value. For $\frac{L_p}{d_n}$, the value of $\eta \approx 0.15$. Therefore, a corrected corelation for $\frac{\delta}{L_p}$, proposed by Abouali and Ahmedi [51] is used for the theoretical prediction of the location of the bow shock :

$$\frac{\delta}{L_p} = \begin{cases} -0.8743\eta^3 + 1.6322\eta^2 - 0.4108\eta + 0.1445, & 0.05 < \eta \leq 0.85 \\ 0.0117\eta^3 - 0.1346\eta^2 + 0.5431\eta + 0.0703, & 0.85 < \eta < 5, \\ 1 - \frac{0.67}{\eta}, & \eta \geq 5. \end{cases} \tag{5.3}$$

Figure 5.6 also shows the bow shock clearly formed before the impactor plate. For the given operating conditions, the distance of the bow shock is measured as

$\delta/L_p = 0.125$. This value of δ/L_p closely agrees with the value of 0.1206 predicted by Equation 5.3.

The bow shock has significant influence on the collection performance of the impactor. The high gradient of pressure across the shock, and the rapid change in direction of the flow act as an obstacle to the flow of particles exiting from the nozzle.

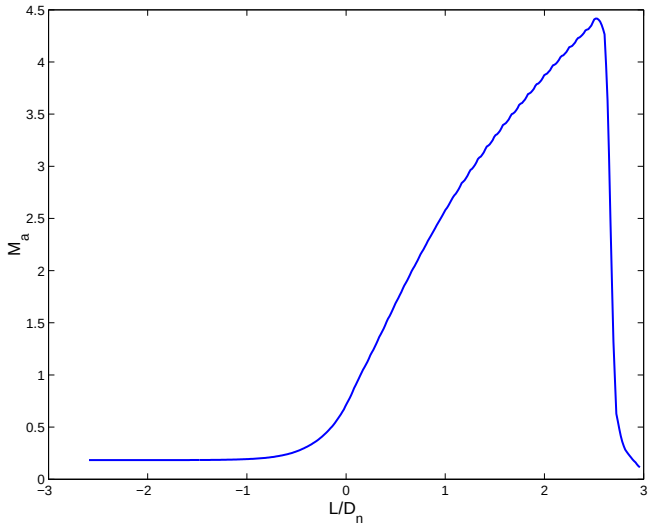

Figure 5.7. Variation of Mach number along the centerline

The particles were introduced into the computational domain through the inlet. The initialization of the particles across the inlet of the axisymmetric mesh should adequately represent uniform initialization across the entire cross-sectional area of the actual nozzle. The particles have been initialized in such a way, that equal number of particles lie in each circular infinitesimal element of the total cross sectional area. The spacing between every consecutive particle represents this circular element. The algorithm for calculating the radial position of every consecutive particle (r_{pos}), is as given below:

$R = Inlet\ radius\ of\ nozzle.$

$A = Cross\ sectional\ area.$

$\Delta A = Area\ of\ elemental\ area\ representing\ each\ particle.$

$N_p = number\ of\ particles.$

$Width\ of\ innermost\ ring\ r_1 = \sqrt{\frac{R^2}{N_p}}$

Since ΔA should remain constant between every particle,

$\Delta A = \pi({r_o}^2 - {r_i}^2)$

$r_o = \sqrt{{r_i}^2 + \frac{\Delta A}{\pi}}$

Thus the position of every particle is calculated by the following iterative procedure:

$r_i = 0;$

for $i = 1 \rightarrow N_p$ **do**

$r_o = \sqrt{{r_i}^2 + \frac{\Delta A}{\pi}}$

$r_{pos} = \frac{1}{2}(r_i + r_o)$

$r_i = r_o$

end for

where r_i and r_o are the inner and outer radius of every consecutive element and r_{pos} is the radial position of each particle at the center of the element.

The "Trap" boundary conditions were used to simulate the collection of the particles on the impactor plate after the impact. Collection efficiency of the device is measured by calculating the ratio of the particles collected on the impactor surface over the total number of particles entering the domain. Figure 5.8 shows typical particle tracks obtained by the Lagrangian solver. The bow shock acts as a sudden obstacle in the path of the flow.

The performace of the impactor plate is measured by the collection efficiency for a given range of particle diameters d_p. The probability of a particular d_p of crossing the shock wave and impacting on the plate surface is directly proportial to its Stokes number S_t.

Collection efficiency results obtained by the present CFD for particle size (1 to 100)nm are being compared to results obtained by Fernandez de la Mora in Figure 5.9. CFD results by Abouali et al (2005) [1] have also been used for comparison.

The CFD results predict a 100% collection efficiency for values of $d_p \geq 10nm$. A cut diameter i.e. the value of d_p which has a collection efficiency of 50%, of 3 nm has been obtained. These results predicted by the numerical solver agree well with the experimental results. This demonstrates the ability of the Lagrangian particle class to accurately model the drag forces acting on sub-micron particles in rarefied conditions. Moreover, the validation results demonstrate the efficiency of *rhoCentralFoam* coupled with the Stokes Cunningham correction factor.

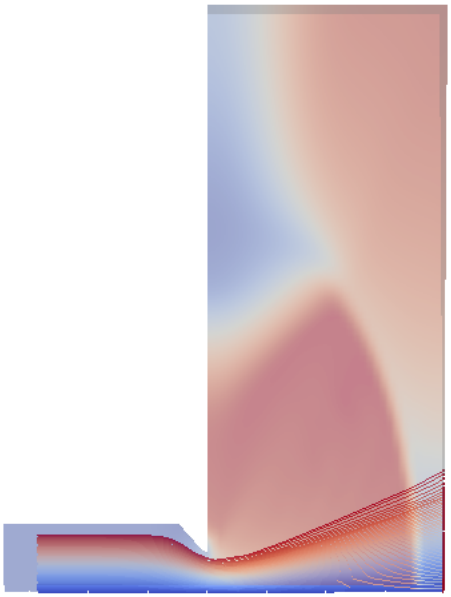

Figure 5.8. Particle tracks for $d_p = 10$ nm.

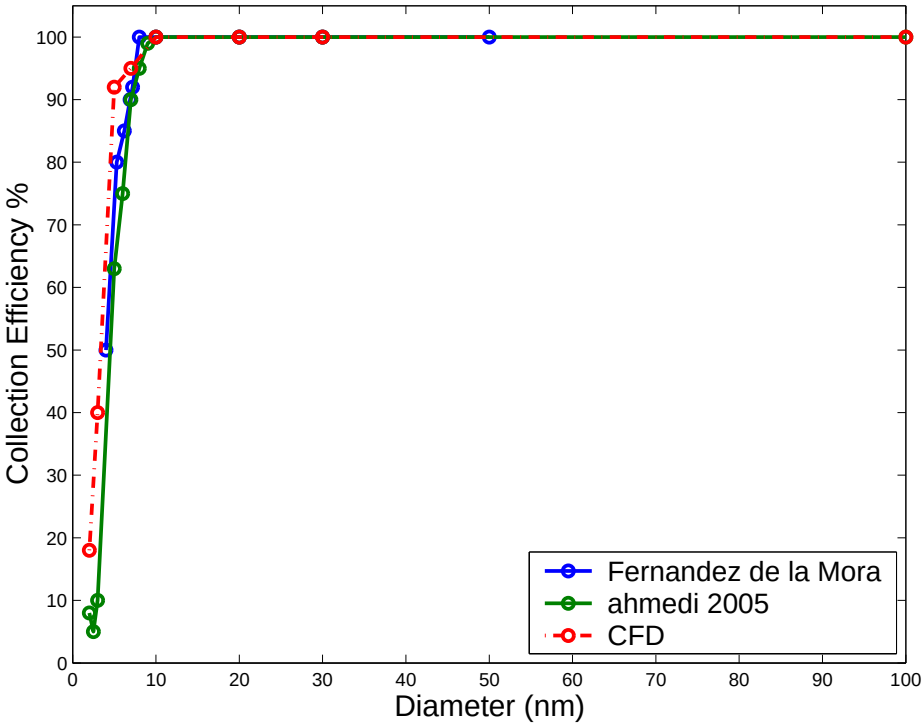

Figure 5.9. Comparison of collection efficiency

CHAPTER 6

RESULTS

6.1 Flow field of the under-expanded jet

In this chapter, computational results of particle focusing obtained by two types of nozzles have been discussed. A straight nozzle and a sharply converging nozzle have been used for this purpose. The nozzles have an outlet diameter $d_n = 5mm$. The straight nozzle has a length of approximately $12mm$. The converging nozzle has an inlet diameter of $8mm$. It has a sharply converging section with a depth of $2mm$. The computational domain of the geometry, is decomposed into an axi-symmetric, Finite-Volume (F-V) mesh of approximately 3000 cells. The mesh has 5 cells across the radius of the mesh. The supersonic under-expanded jet has been simulated using *rhoCentralFoam*. Particle trajectories in the resulting flow have been studied by the Lagrangian particle class, implementing the Cunningham correction factor while calculating the drag forces

Inlet boundary conditions represent reservoir conditions having total pressure of $101325Pa$. Non-reflective boundary conditions are used at the outlet with a fixed value of $101Pa$. The code, which is transient, is run until the solution reaches a steady state.

6.1.1 Straight nozzle

The steady state results for the straight nozzle can be seen in Fig 6.1. The air experiences a pressure drop as it enters the nozzle channel. Due to the sudden drop in the flow area, a vena-contracta region is formed at the inlet. Here, the air is deflected

towards the centerline of the nozzle (Figure 6.3). As it exits the nozzle, it rapidly expands to match the back pressure.

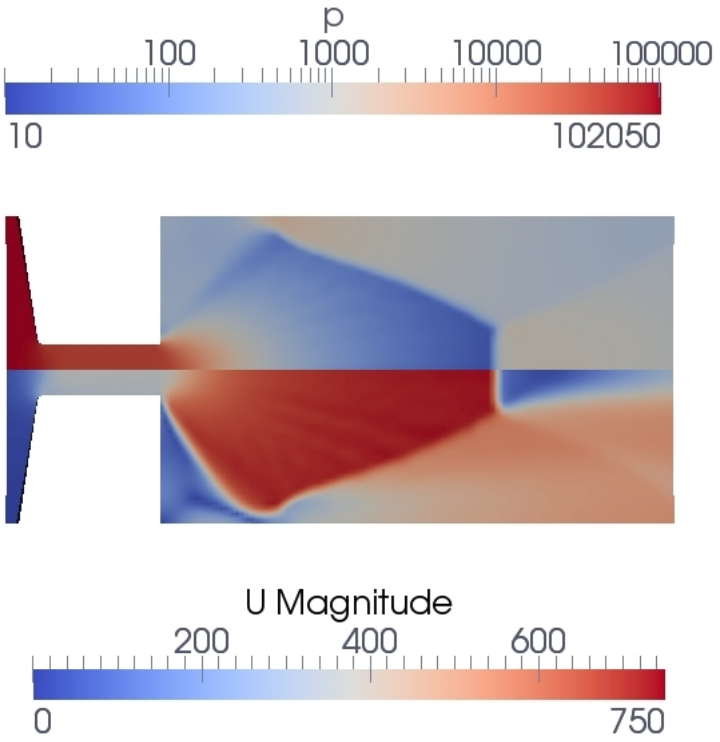

Figure 6.1. Pressure and velocity contours for the straight nozzle.

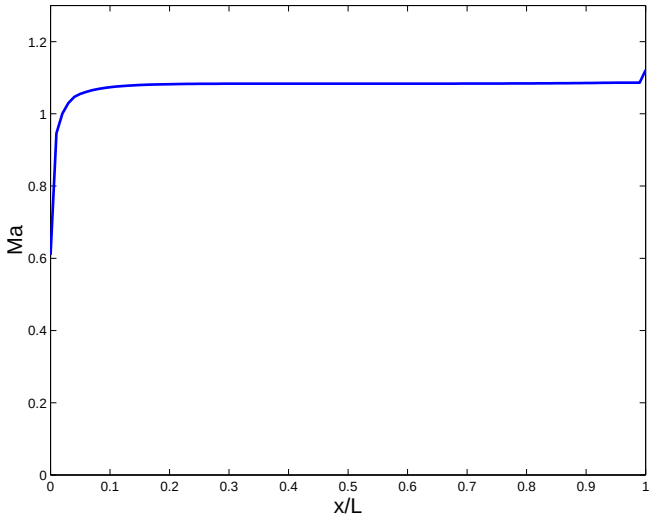

Figure 6.2. Mach number variations across the centerline, along the length of the straight duct

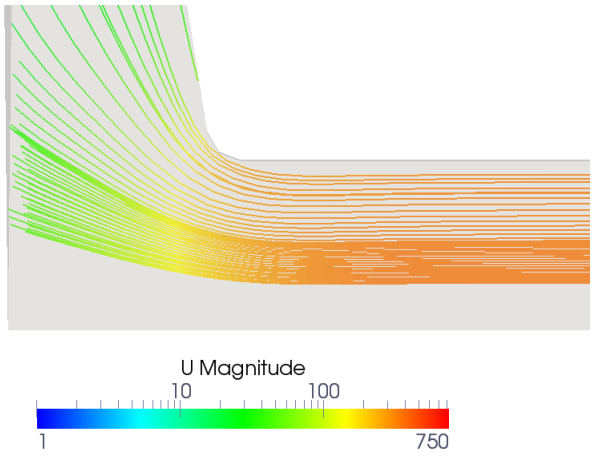

Figure 6.3. Vena-contracta experienced at nozzle inlet.

The rapid expansion results in the formation of an under-expanded jet. The core of this jet is characterized by an extremely low pressure region bounded by strong shocks. A normal shock, the Mach disc is seen downstream. The region immediately downstream of the Mach disc is a stagnation region with an extremely low velocity. Figure 6.2 shows the variations of the Mach number, calculated along the centerline of the flow field. A sharp acceleration is seen at the inlet of the nozzle reaching $M = 1$. Further downstream, the Mach number exceeds unity, reaching a value of 1.08 throughout the length. According to the $1 - D$ Fanno flow analysis [42], the flow inside the straight nozzle must indeed not exceed $M = 1$. The Mach number variation in the nozzle is found to be independent of the density of the grid prompting the need to search studies that recorded similar observations.

Murphy and Miller (1984) [30] recorded measurements of Mach number of the flow, in the downstream region of a straight and a converging nozzle, starting from a point right outside the nozzle exit. They observed that while the flow through converging nozzle reached $M = 1$ at a distance of $0.25 * D_n$ from the exit, flow through a capillary (straight) nozzle obtained $M \approx 1.4$ at the same length. The measured the 'sonic surface' to be occuring atleast one diameter upstream of nozzle exit. These values were recorded by pitot tube. However, the authours could not

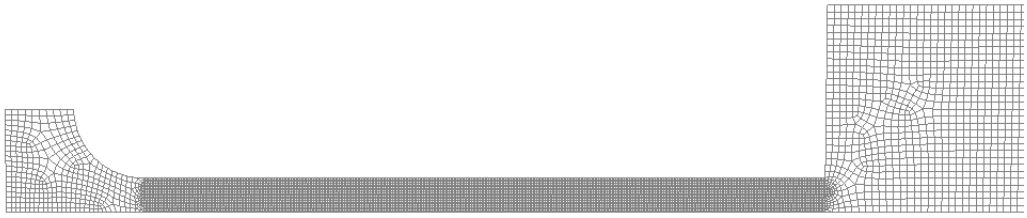

Figure 6.4. Computational mesh representing nozzle-duct assembly used by [24, 26]

explain the reason for this anamoly in their paper. Beyond a short distance along the axis, the profile of the jet did not seem to be dependent on the nozzle geometry.

Kubo et al. (2010) [24] observed the flow inside the duct section reaching $M > 1$, near the exit, in their experimental investigation of choked flow in straight ducts. Lijo et al. (2009) [26] performed detailed numerical investigations of choked flow inside straight ducts and compare them with Kubo's observations. The length of the duct was varied in order to observe the influence of the $\frac{L}{D_n}$ ratio on the flow. Lijo et al. confirmed the value of M to be greater than 1, near the exit. Both the works attributed this deviation to the viscous effects near the exit region, which reduced the effective cross-sectional area for the flow. Moreover, the thinning of the boundary layer near the exit provided a diverging section for the flow, causing the value of M to rise above 1. In both the studies, the air enters the straight duct through a gradually converging nozzle. Figure 6.4 shows the computational mesh of the nozzle-duct section. The inlet nozzle has a circular profile, with a radius $R = 2 * D_n$.

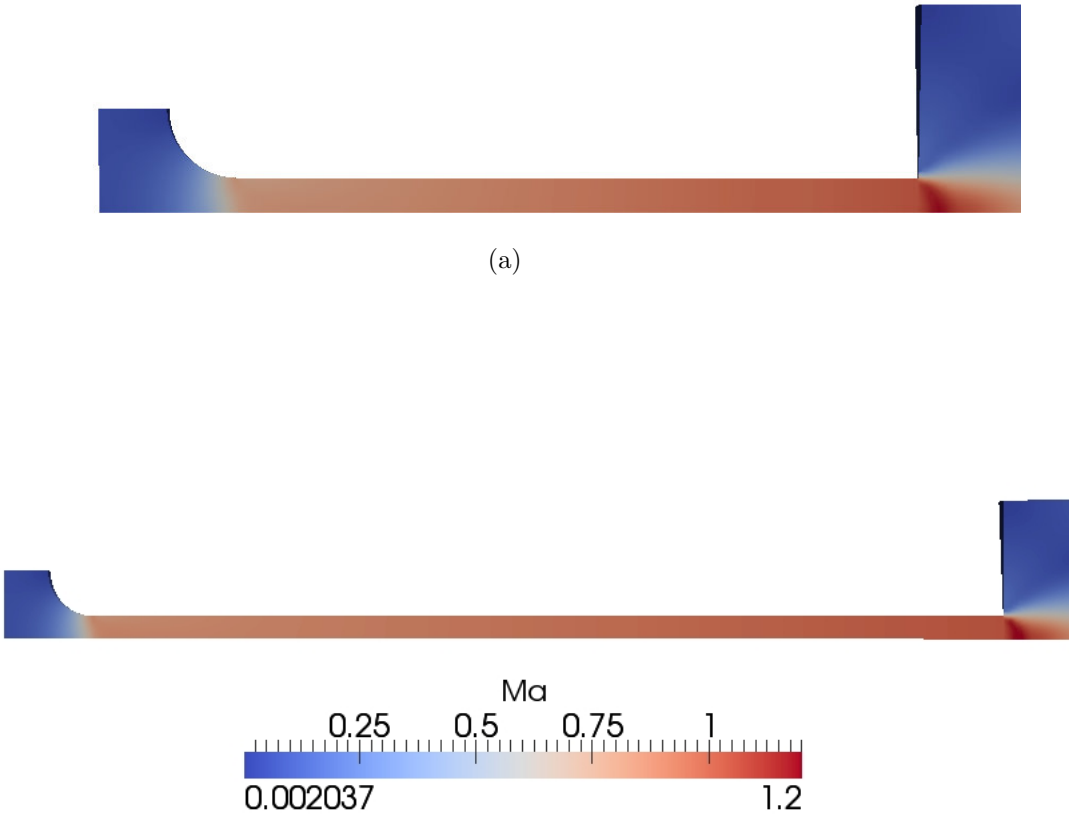

(a)

(b)

Figure 6.5. Steady state Mach number contours (a) $\frac{L}{D_n} = 10$ (b) $\frac{L}{D_n} = 20$

Results by Lijo et al. and Kubo et al. are reproduced by *rhoCentralFoam* in Figure 6.5 for the purpose of validation. The operating conditions are the same as used in both the studies. Pressure ratio, $\frac{P_b}{P_o} = 0.435$ has been applied across the domain. Simulations have been performed for $\frac{L}{D_n}$ ratios of 10 and 20. Figure 6.6 shows the steady state results of Mach number contours obtained by *rhoCentralFoam*, for $\frac{L}{D_n} = 10, 20$.

The flow starts with a subsonic velocity, with M rising to a value slightly lower than 1 at the inlet of the straight duct. As the flow approaches the exit, $M = 1$ is reached at a point, approximately $(80 - 90\%)$ of the total length of the ducts. This is consistent with the results of Kubo et al. [24] and Lijo et al. [26].

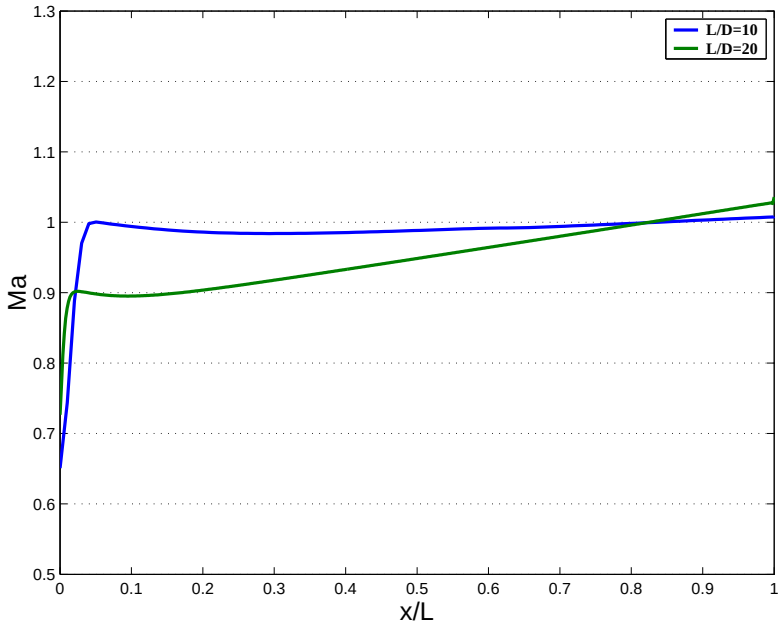

Figure 6.6. Mach number variations in straight duct for $\frac{L}{D_n} = 10, 20$.

However, the trend of the Mach number varies a lot for the flow entering the duct through a sharply converging nozzle (this is the nozzle geometry used in the thesis). The pressure and velocity contours and the Mach number variation across the centerline along the length of the straight duct, obtained from the steady state results are shown in Figures 6.1 and 6.2 respectively. The straight duct in this simulation has a $\frac{L}{D_n} \approx 4$. The vena-contracta at the duct inlet, due to the sudden contraction in the cross sectional area, causes the M to exceed 1 at the inlet of the duct. The centerline Mach number remains above 1 throughout the length of the duct. As the flow nears the exit, M rises to reach a high value downstream. Similar trends have been observed for a $\frac{L}{D_n} = 20$, with operating conditions matching experimental conditions ($\frac{P_b}{P_o} = 0.435$).

In the results seen in Figure 6.5(a) and 6.5(b), the flow chokes only at a point close to the exit of the duct, where it reaches $M = 1$. At the inlet of the duct, the flow does not accelerate to reach $M = 1$, even though for the case of $\frac{L}{D_n} = 10$ it reaches a value very close to unity, i.e. $M = 0.99$. Hence, no choking is observed at

this point. However, in Figure 6.1, the flow already attains choking at the point of the vena-contracta.

The deviation of the compressible flow in the straight duct from the Fanno flow theory may therefore be explained by the geometric factors rather than numerical error. The velocity profiles of the flow in the duct and near the exit are found to be sensitive to the inlet profiles of the nozzles and the length of the duct. As the flow enters the straight nozzle in Figure 6.1, it experiences a sharp acceleration due to the sudden contraction in cross-sectional area, resulting in it reaching $M > 1$. The vena contracta at the inlet seems to be playing a role similar to the one played by the boundary layer thinning at the exit, by offering a diverging passage for the flow, causing M to exceed unity.

6.1.2 Converging nozzle

The steady state pressure and velocity contours of the under-expanded jet obtained by a sharply converging nozzle can be seen in Figure 6.7. The change in values of the properties in the converging section is a function of the change in cross-sectional area. This relation can be expressed in Equations (2.4 - 2.7). Beyond the exit, the gas expands rapidly and the properties are identical to the ones observed for the straight nozzles. However, differences can be observed in the conditions upstream of the nozzle outlet. Figure 6.8 shows the Mach number variation across the centerline, calcutated for the converging nozzle. The flow experiences an acceleration as it enters the converging section. The velocity increases gradually reaching $M = 1$ at the minimum cross section which is also the exit.

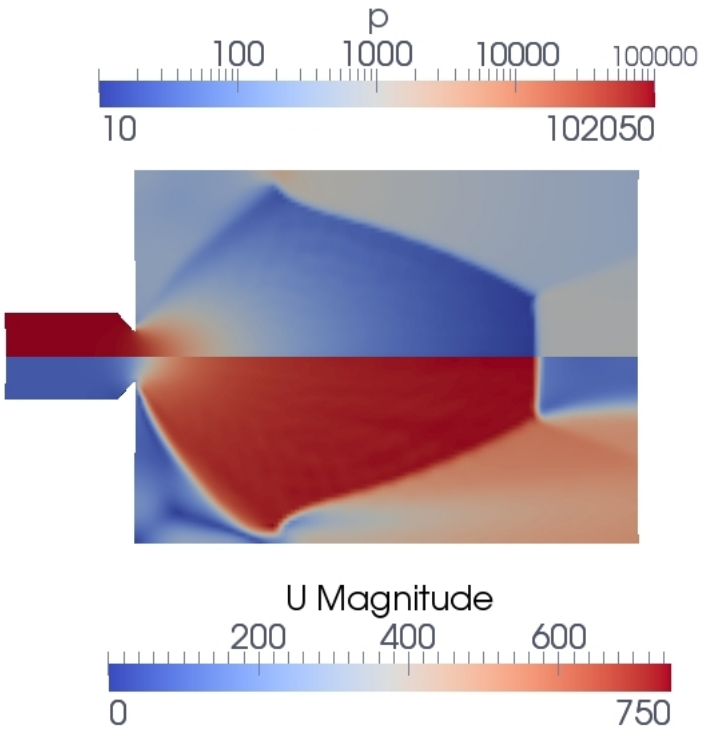

Figure 6.7. Pressure and velocity contours for the converging nozzle.

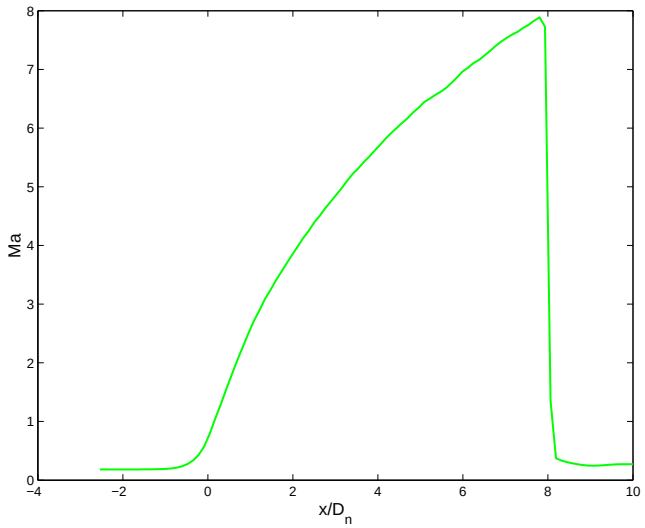

Figure 6.8. Mach number variations across the centerline for the converging nozzle.

6.2 Particle phase

In order to study the particle trajectories for particle diameters of various sizes in the micron-submicron range, particle streams were initialized in the steady state solution of the single phase under-expanded jet. The particles were initialized uniformly across the inlet of the domain. A uniform value of particle diameter d_p has been used for each simulation. The range of d_p varies from 0.1-10 μm. The particle drag force was calculated using the Stokes-Cunningham correction factor to account for effects due to rarefaction. The width of the particle beams is been measured for d_p ranging from 0.1 μm to 10 μm. The extent of spread for each value of d_p has been measured in terms of the radial distance of the particles from the centerline, using a probability density function (PDF). A PDF is a function that describes the probability of an event to occur at a given point. In this case, the Weibull PDF [48] shall be used to predict the probability of a particle of a given diameter to be spread within a particular distance from the centerline. The Weibull probability distribution function is given by the following expression:

$$f(x,c,k) = \begin{cases} \frac{k}{c}(\frac{x}{c})^{k-1}e^{-(\frac{x}{c})^k} & x \geq 0 \\ 0 & x < 0 \end{cases} \tag{6.1}$$

where k is the shape parameter and c is the scale parameter of the function. Both are defined as follows:

$$k = \left(\frac{\sigma}{\mu}\right)^{-1.086} \tag{6.2}$$

$$c = \mu\left(0.568 + \frac{0.433}{k}\right)^{-\frac{1}{k}} \tag{6.3}$$

where σ is the standard deviation of the range of data and μ is it's mean.

The accuracy of the PDF can be verified by comparing it with a histogram of the same data. The histogram measures the frequency of occurance of a particular event. In this case, the histogram would measure the frequency of radial position

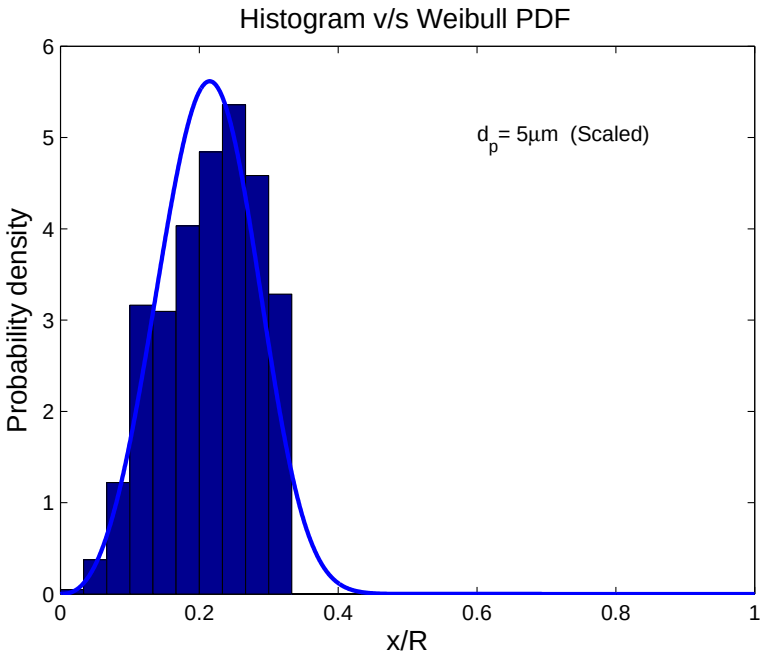

Figure 6.9. Histogram

of the particle to fall in a range. The events, i.e. the range of the radial distance from the centerline is divided into number of equally sized bins. Figure 6.9 shows a histogram plotted for $100,000$ particles along with a Weibull PDF for the data.

6.2.1 Particle focusing by a straight nozzle

The particle trajectories for values of $d_p = 0.1\ \mu m$, $1\ \mu m$ and $5\ \mu m$ calculated by the Cunningham correction factor, C_c can be seen in Fig 6.10. The width of the particle beams can be clearly seen to varying for each value of d_p. This variation for the entire range of d_p used is being plotted using a Weibull PDF in Fig 6.11.

As the air from the reservoir conditions enters the nozzle, it forms a vena-contracta region at the inlet. The flow experiences a sharp acceleration due to the sudden change in area. The response of the particles in the flow to this acceleration varies for every value of d_p. The smallest particles that are suspended in the air have a $d_p = 0.1\ \mu m$. They remain closely coupled with the gas streamlines as the flow enters the nozzle. After passing through the vena-contracta region, they continue to follow pathlines parallel to the axis. As the flow expands rapidly to the extremely low back pressure P_b, the particles again closely follow the streamlines and form wide beams in the expansion chamber. As the value of d_p approaches $1\ \mu m$, the particles are focused very close to the axis. For $d_p = 1\ \mu m$, the particle beam remains tighly focused close to the centerline. As d_p rises above $1\ \mu m$, the particles tend to cross the centerline at a point very close to the nozzle exit. This results in increasing width of the beams downstream. This behavior is because of the particles having $S_t \gg 1$. Such behavior for particles having a higher S_t has been observed by Fernandez de la Mora et al [15] in their experimental investigation of focusing aerosol beams in a thin plate impact separator. Due to the extremely narrow distribution for $d_p = 1\mu m$, the PDF figure for their positions is plotted separately in Figure 6.11(a). The PDFs for the other sizes of d_p are plotted in Figure 6.11(b).

The focusing performance of a particular nozzle geometry can be characterized by the value of S_t for optimally focused particle diameter, d_p. The approximate values of S_t (Equation 2.2) based obtained assuming sonic gas velocity at the inlet are provided in Table 6.2.1.

Table 6.1. S_t at nozzle inlet

$d_p(\mu m)$	Stokes Number, S_t
0.1	0.0209
0.2	0.0487
0.4	0.1312
0.7	0.3287
1	**0.6156**
2	2.2110
5	12.8805

The particle pathlines in Figure 6.10 also represent the translational velocity of the particles U_p, as a function of their position. Even though the particles are initialized with an initial velocity $U_i = 0$, the magnitude of their velocity in the nozzle and the under-expanded jet varies for every value of particle diameter. For $d_p = 0.1\mu m$, the particle velocity remains closely coupled to that of the gas phase. As they enter the nozzle, they experience a sharp acceleration to a value of $U_p \approx 300m/s$. As the jet exits from the nozzle, the particles exprerience further acceleration to a maximum value of $U_p \approx 550m/s$. This velocity is reached at a distance approximately equal to the diameter of the nozzle. The particles lose some velocity as the cross the Mach disc.

Particles with $d_p = 1\mu m$ experience the similar trend of acceleration in the nozzle and in the expansion chamber. However, the magnitude of U_p reached is lower than that attained for $d_p = 0.1\mu m$ throughout the flow. A maximum value of $U_p \approx 350m/s$ is reached outside the exit of the nozzle. The presence of the Mach disc does not seem to have any influence on the velocity of the particles.

For $d_p = 5\mu m$, the maximum velocity drops further. The acceleration experienced by these particles at the nozzle inlet is lower than that observed for the smaller diameters. Even as they leave the nozzle, the maximum U_p attained remains on the order of $150 m/s$.

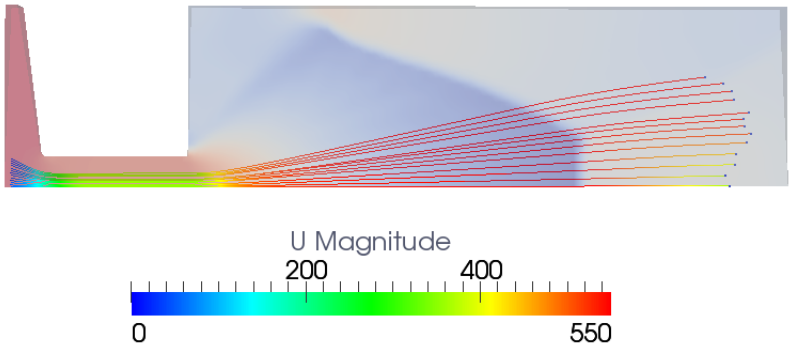

(a)

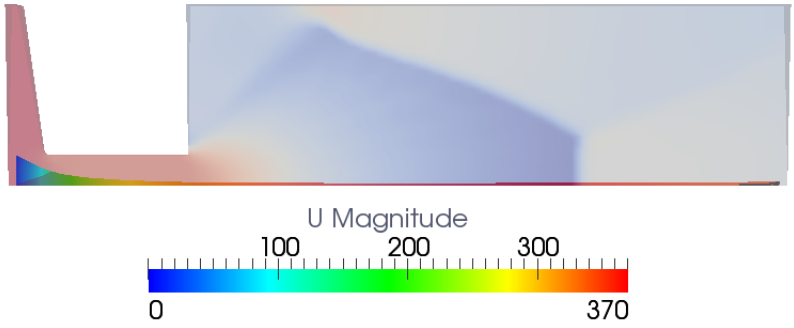

(b)

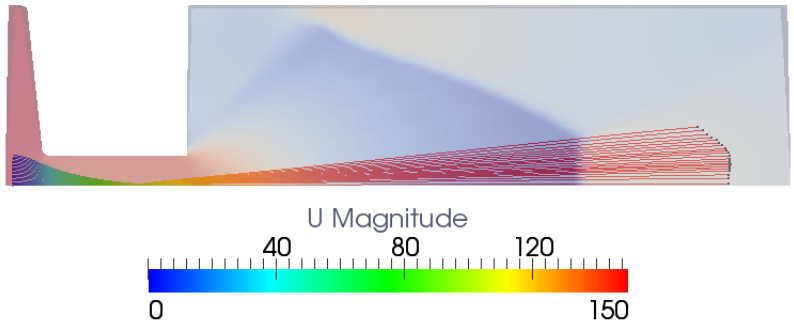

(c)

Figure 6.10. Pathlines for (a) d_p=0.1 μm, (b) d_p=1 μm and (c) d_p=5 μm for the straight nozzle. The legend represents velocity of the particle trajectories.

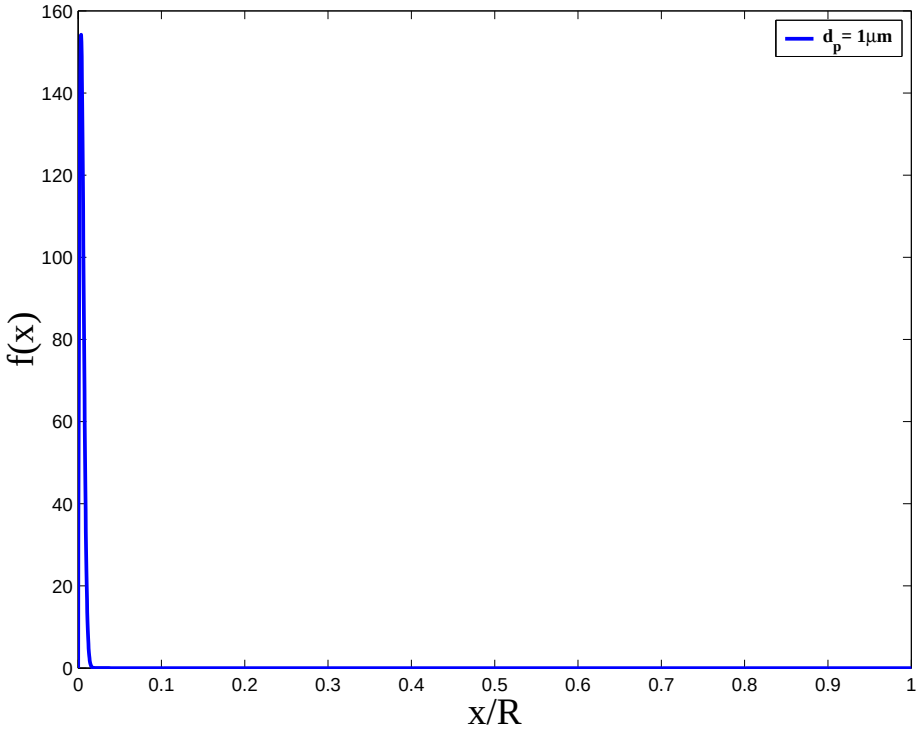

(a)

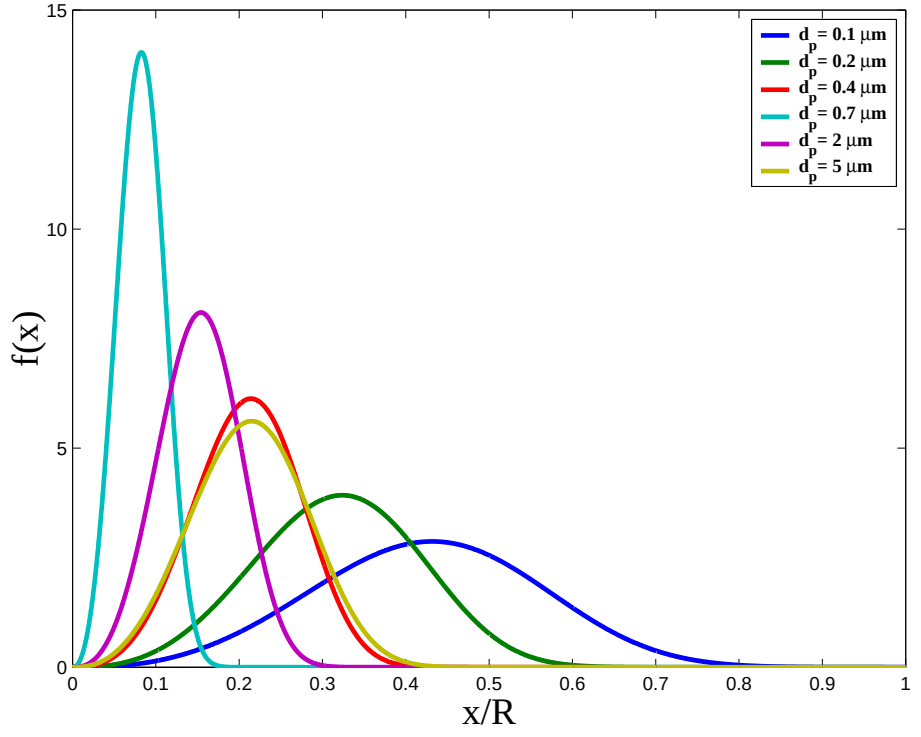

(b)

Figure 6.11. Weibull PDF for particle focusing by the straight nozzle

6.2.2 Particle focusing by a convergent nozzle

Fig.6.12 shows the particle pathlines obtained by a convergent nozzle. The focusing performance of the convergent nozzle is less efficient than the one obtained by the straight nozzle for the identical range of d_p. The acceleration experienced by the gas at it enters the convergent section of the nozzle is less rapid compared to the straight nozzle. Therefore the tendency of the particles to separate from the gas streamlines is lesser. The distribution of the particle beam around the centerline has been measured using a Weibull PDF and plotted in (Figure 6.14).

Smaller particles that remain closely coupled to the gas streamlines due to their low inertia, closely follow the nozzle geometry. However for $d_p \approx 1\mu m$, the particles impact on the converging section. This collision results in the random crossing of the centerline by these particles, preventing the formation of continous particle beams in the downstream region (Figure 6.13). Particles that cross the centerline at wide angles approach the walls of the expansion chamber.

The particle velocity U_p can also be observed from the pathlines in Figure 6.12. A similar trend of U_p varying with the particle diameter can be seen. The maximum velocity attained by the respective particles in the expansion chamber is approximately equal to that attained by the straight nozzle. However, the acceleration experienced by the particles inside the converging section is not the same as for the straight nozzle.

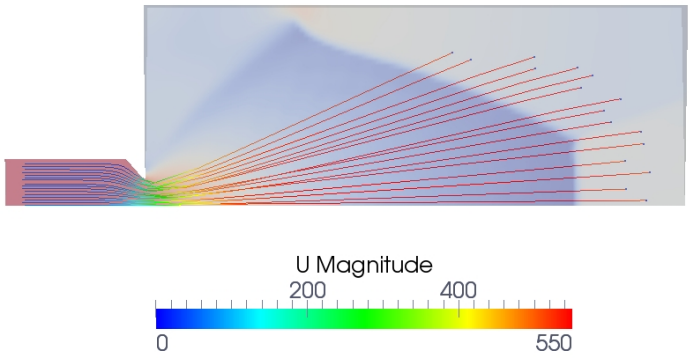

(a)

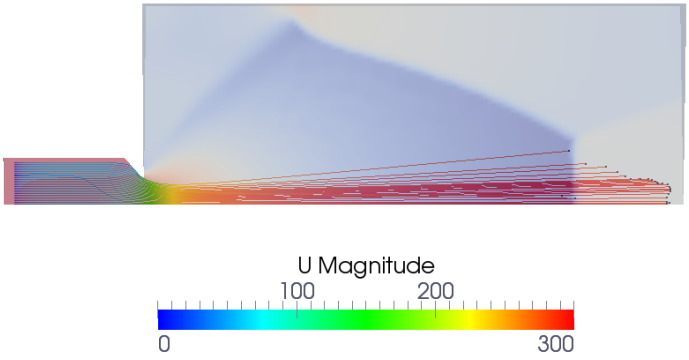

(b)

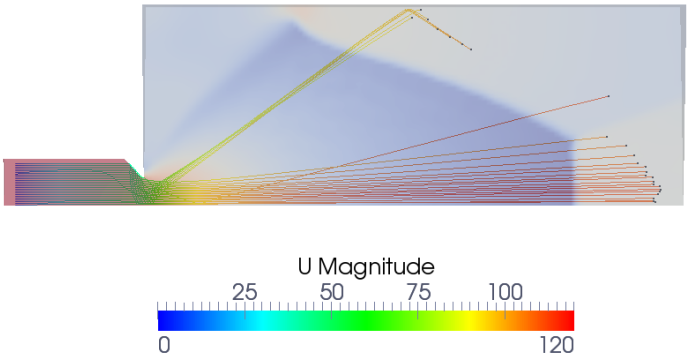

(c)

Figure 6.12. Pathlines for (a) d_p=0.1 μm, (b) d_p=1 μm and (c) d_p=5 μm for the convergent nozzle case. The legend represents velocity of the particle trajectories.

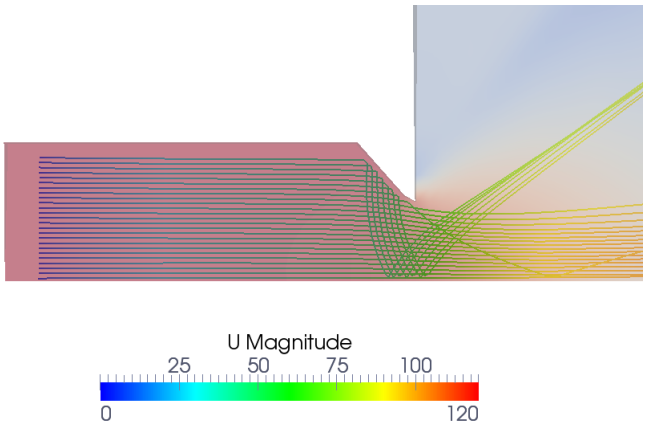

Figure 6.13. Enlarged view of particles having $dp = 5\mu m$ crossing the centerline

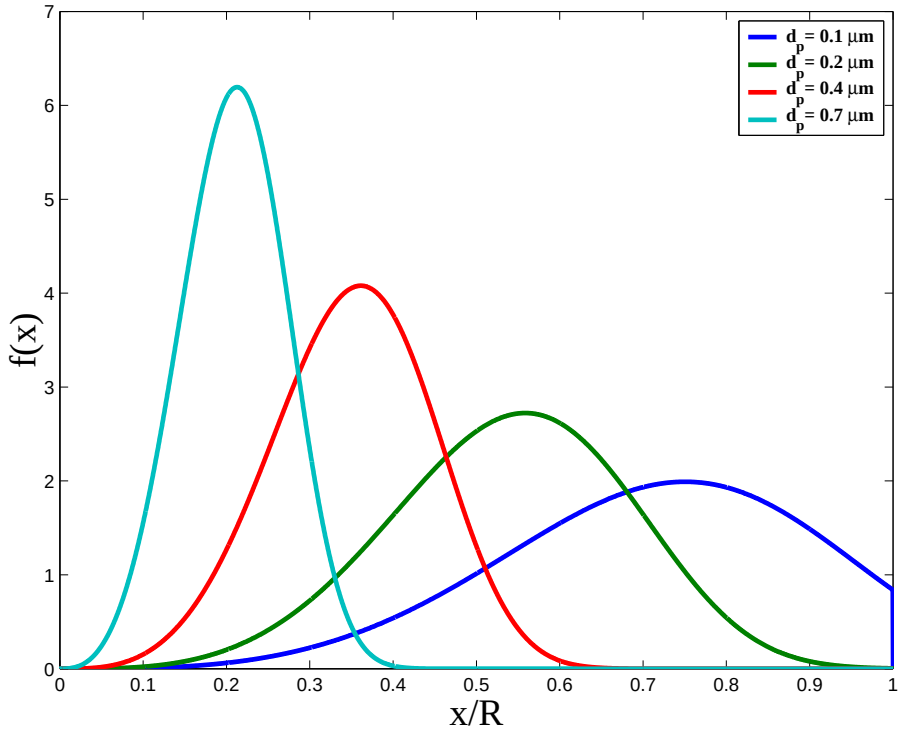

(a)

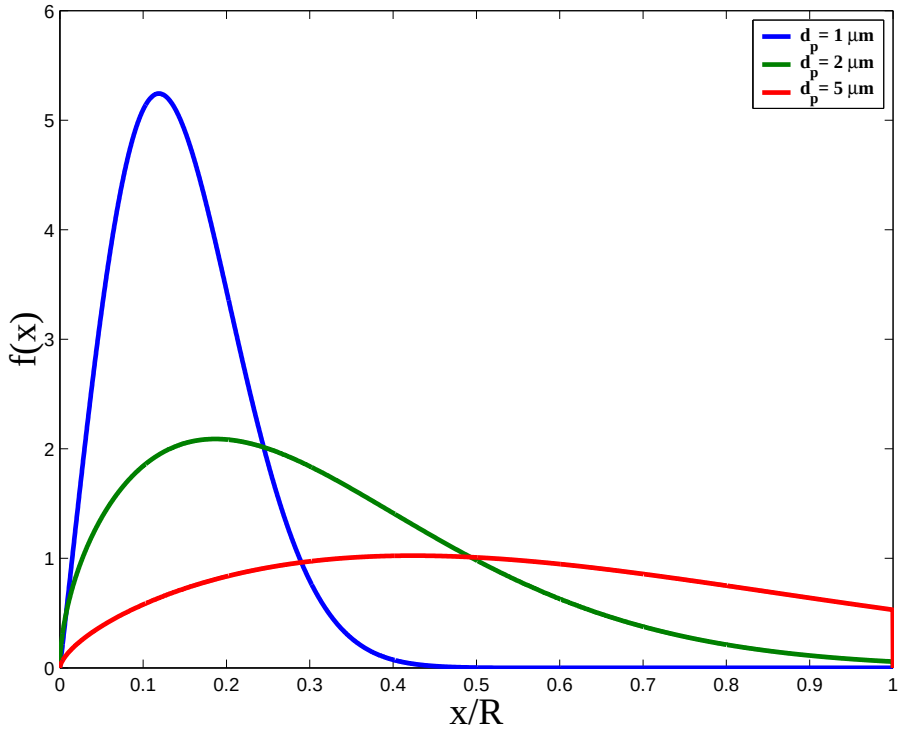

(b)

Figure 6.14. Weibull PDF for particle focusing by a convergent nozzle

6.3 Conclusion

The particle trajectories calculated using CFD demonstrate that the straight nozzle geometry is more efficient towards focusing particles in an under-expanded free jet. The focusing is obtained for a very narrow range of particle diameters, which is of the order of 1 μm for the straight nozzle applied here. This performance can be characterized by an optimum Stokes number in the order of 0.6. Experimental results by Fernandez de la Mora et al [15] observed optimum focusing Stokes number in the similar range. The width of this particle beam is less than 0.1% of the nozzle diameter. Similar results were obtained by Fernandez de la Mora [15]. Dahneke and Chang [8] observed best focusing for particles with an optimum value of an inertia parameter 'β' which is closely related to the Stokes number.

The focusing performance of the sharply converging nozzle is much less efficient than the one obtained for the straight nozzle. Even though the expansion of the gas from the reservoir pressure to the rarefied background pressure is largely independent of the nozzle geometry, the optimum separation of particles seems to be dependent to a great extent on the nozzle inlet conditions. By providing a high acceleration to the flow at its inlet due to the sudden change in cross-sectional area, the straight nozzle is better suited for this application than the converging nozzle. Moreover, straight nozzles are easier to design and fabricate.

The particles that are tightly focused along the centerline can be separated from the rest of the flow by using apparatus like a skimmer or a probe placed coaxially. Most researchers note that the ideal position for such a skimmer would be at a distance upstream of the Mach disc [39, 40]. Moreover, additional focusing has been observed to have been brought about by the skimmers due to the inertial effects experienced at their inlets.

We thereby conclude that aerodynamic separation of particles offers a very effective and simple way to separate and collect particles belonging to the sub-micron range.

BIBLIOGRAPHY

[1] Abouali, Omid, and Ahmadi, Goodarz. A model for supersonic and hypersonic impactors for nanoparticles. *Journal of Nanoparticle Research 7* (2005), 75–88. 10.1007/s11051-004-7910-3.

[2] Addy, A.L. Effects of axisymmetric sonic nozzle geometry on mach disc characteristics. *AIAA Journal 19*, 1 (January 1981), 121–122.

[3] Anderson, John David. *Modern compressible flow : with historical perspective*. McGraw-Hill, New York, 1990. ID: 19981293.

[4] Ashkenas, H., and Sherman, F. S. The Structure and Utilization of Supersonic Free Jets in Low Density Wind Tunnels. In *Rarefied Gas Dynamics, Volume 2* (1965), J. H. de Leeuw, Ed., pp. 84–+.

[5] Becker, E. W., Bier, W., Ehrfeld, W., Schubert, K., Schtte, R., and Seidel, D. Uranium enrichment by the separation-nozzle process. *Naturwissenschaften 63* (1976), 407–411. 10.1007/BF00599408.

[6] Becker, E.W., and Bier, K. *Z. Naturforsh. Teil A9*, 5 (1954), 975.

[7] Becker, E.W., Bier, K., and Burghoff, H. *Z. Naturforsh. Teil A10* (1955), 565.

[8] Cheng, Y.S., and Dahneke, B.E. Properties of continuum source particle beams: Ii. beams generated in capillary expansions. *Journal of Aerosol Science 10*, 4 (1979), 363 – 368.

[9] Colella, Phillip, and Woodward, Paul R. The piecewise parabolic method (ppm) for gas-dynamical simulations. *Journal of Computational Physics 54*, 1 (1984), 174 – 201.

[10] Crist, S., Sherman, P.M., and Glass, D.R. Study of highly underexpanded sonic jet. *AIAA Journal 4*, 1 (1966), 68 – 71.

[11] Cunningham, E. On the velocity of steady fall of spherical particles through fluid medium. *Proceedings of the Royal Society of London. Series A, Containing Papers of a Mathematical and Physical Character 83*, 563 (1910), pp. 357–365.

[12] de la Mora, J. Fernandez, Hering, S.V., Rao, N., and McMurry, P.H. Hypersonic impaction of ultrafine particles. *Journal of Aerosol Science 21*, 2 (1990), 169 – 187.

[13] Dykhuizen, R., and Smith, M. Gas dynamic principles of cold spray. *Journal of Thermal Spray Technology 7* (1998), 205–212. 10.1361/105996398770350945.

[14] Fenn, John B. Mass spectrometric implications of high-pressure ion sources. *International Journal of Mass Spectrometry 200*, 1-3 (2000), 459 – 478.

[15] Fernandez de La Mora, J., and Rosell-Llompart, J. Aerodynamic focusing of heavy molecules in seeded supersonic jets. *The Journal of Chemical Physics 91* (Aug. 1989), 2603–2615.

[16] Fluent. *Fluent 6.2 Tutorial Guide*. Fluent Inc., Centerra Resource Park, 10 Cavendish Court, Lebanon, NH 03766, USA, January 2005.

[17] Frain, Matthew. Study of inertial impingement type gas/particle separator. Master's thesis, University of Massachusetts at Amherst, 2000.

[18] Greenshields, Christopher J., Weller, Henry G., Gasparini, Luca, and Reese, Jason M. - implementation of semi-discrete, non-staggered central schemes in a colocated, polyhedral, finite volume framework, for high-speed viscous flows. *International Journal for Numerical Methods in Fluids - 63*, - 1 (- 2010), – 1–21.

[19] Haider, A., and Levenspiel, O. Drag coefficient and terminal velocity of spherical and nonspherical particles. *Powder Technology 58*, 1 (1989), 63 – 70.

[20] Harten, Ami. High resolution schemes for hyperbolic conservation laws. *Journal of Computational Physics 49*, 3 (1983), 357 – 393.

[21] Harten, Ami, Engquist, Bjorn, Osher, Stanley, and Chakravarthy, Sukumar R. Uniformly high order accurate essentially non-oscillatory schemes, iii. *Journal of Computational Physics 71*, 2 (1987), 231 – 303.

[22] Henderson, C.B. Drag coefficient of spheres in continuum and rarefied flows. *AIAA J. 14*, 6 (1976), 707–708.

[23] Kantrowitz, Arthur, and Grey, Jerry. A high intensity source for the molecular beam. part i. theoretical. *Review of Scientific Instruments 22*, 5 (May 1951), 328 –332.

[24] Kubo, Kazunori, Miyazato, Yoshiaki, and Matsuo, Kazuyasu. Study of choked flows through a convergent nozzle. *Journal of Thermal Science 19* (2010), 193–197. 10.1007/s11630-010-0193-3.

[25] Kurganov, Alexander, Noelle, Sebastian, and Petrova, Guergana. Semidiscrete central-upwind schemes for hyperbolic conservation laws and hamilton-jacobi equations. *SIAM Journal on Scientific Computing 23*, 3 (2002), 707–740. Compilation and indexing terms, Copyright 2010 Elsevier Inc.; M1: Compendex; undefined.

[26] Lijo, V., Kim, H.D., and Setoguchi, T. Analysis of choked viscous flows through a constant area duct. *Proceedings of the Institution of Mechanical Engineers, Part G: Journal of Aerospace Engineering 224*, 11 (2010), 1151 – 1162.

[27] Matsuo, S., Tanaka, M., Otobe, Y., Kashimura, H., Kim, H.D., and Setoguchi, T. Effect of axisymmetric sonic nozzle geometry on characteristics of supersonic air jet. *Journal of Thermal Science 13*, 2 (2004), 121–126.

[28] Menon, N., and Skews, B.W. Effect of nozzle inlet geometry on underexpanded supersonic jet characteristics. In *Shock Waves*, Klaus Hannemann and Friedrich Seiler, Eds. Springer Berlin Heidelberg, 2009, pp. 955–960.

[29] Morsi, S. A., and Alexander, A. J. An investigation of particle trajectories in two-phase flow systems. *Journal of Fluid Mechanics 55*, 02 (1972), 193–208.

[30] Murphy, Hylton R., and Miller, David R. Effects of nozzle geometry on kinetics in free-jet expansions. *The Journal of Physical Chemistry 88*, 20 (1984), 4474–4478.

[31] Musgrove, Grant O., Barringer, Michael D., Thole, Karen A., Grover, Eric, and Barker, Joseph. Computational design of a louver particle separator for gas turbine engines. *ASME Conference Proceedings 2009*, 48845 (2009), 1313–1323.

[32] Nessyahu, Haim, and Tadmor, Eitan. Non-oscillatory central differencing for hyperbolic conservation laws. *Journal of Computational Physics 87*, 2 (1990), 408 – 463.

[33] OpenFOAM. *OpenFOAM © User Guide*. OpenCFD Ltd, OpenCFD Ltd 9 Albert Road Caversham Reading Berkshire RG4 7AN UK, 2010.

[34] Otobe, Y., Kashimura, H., Matsuo, S., Setoguchib, T., and Kim, H.D. Influence of nozzle geometry on the near-field structure of a highly underexpanded sonic jet. *Journal of Fluids and Structures 24*, 2 (February 2008), 281–293.

[35] Papyrin, A., and Blose, R. Cold spray technology: From rd to commercial applications. *Materials Technology 18*, 2 (2003), 73 – 78. Cold spray technology;Commercial applications;Commercialization strategy;.

[36] Pauly, Hans. *Atom, molecule, and cluster beams. I, Basic theory, production and detection of thermal energy beams*. Springer, Berlin; New York, 2000. ID: 46331673.

[37] Poinsot, T. J., and Lelef, S. K. Boundary conditions for direct simulations of compressible viscous flows. *Journal of Computational Physics 101*, 1 (1992), 104 – 129.

[38] Poulton, P., and Cole, B.N. An experimental and numerical investigation of louvred inertia air filter performance. *Institution of Mechanical Engineers* (1981), 161–170.

[39] Reis, Victor H., and Fenn, John B. Separation of gas mixtures in supersonic jets. *The Journal of Chemical Physics 39*, 12 (1963), 3240–3250.

[40] Scoles, Giacinto. *Atomic and molecular beam methods*. Oxford University Press, New York, 1988. ID: 14931494.

[41] Serafini, J.S. Impingement of water droplets on wedges and double-wedge airfoils at supersonic speeds. *National Advisory Committee for Aeronautics – Reports* (1954), 24 –.

[42] Shapiro, Ascher H. *The dynamics and thermodynamics of compressible fluid flow*. Ronald Press Co., New York, 1953. ID: 480618.

[43] Sommerfeld, M. The structure of particle-laden, underexpanded free jets. *Shock Waves 3* (1994), 299–311. 10.1007/BF01415828.

[44] Stokes, George Gabriel. *On the Effect of the Internal Friction of Fluids on the Motion of Pendulums*. Cambridge University Press, 1851.

[45] Tedeschi, G., Gouin, H., and Elena, M. Motion of tracer particles in supersonic flows. *Experiments in Fluids 26* (1999), 288–296. 10.1007/s003480050291.

[46] van Leer, Bram. Towards the ultimate conservative difference scheme. v. a second-order sequel to godunov's method. *Journal of Computational Physics 32*, 1 (1979), 101 – 136.

[47] Versteeg, H. K., and Malalasekera, W. *An Introduction to Computational Fluid Dynamics: The Finite Volume Method*. Pearson Education Ltd., Harlow, England; New York, 2007. ID: 76821177.

[48] Weibull, W. Statistical distribution function of wide applicability. *American Society of Mechanical Engineers – Transactions – Journal of Applied Mechanics 18*, 3 (1951), 293 – 297.

[49] Witman, A. A study of a sub-atmospheric impact separator for the collection and classification of sub-micron particles. Master's thesis, University of Massachusetts at Amherst, 2005.

[50] Yee, H. C. Explicit and implicit multidimensional compact high-resolution shock-capturing methods: Formulation. *Journal of Computational Physics 131*, 1 (1997), 216 – 216.

[51] Zare, Azam, Abouali, Omid, and Ahmadi, Goodarz. Computational investigation of airflow, shock wave and nano-particle separation in supersonic and hypersonic impactors. *Journal of Aerosol Science 38*, 10 (2007), 1015 – 1030.